AWARD NUMBER: W81XWH-14-1-0616

TITLE: Spinal Cord Injury-Induced Dysautonomia via Plasticity in Paravertebral Sympathetic Postganglionic

PRINCIPAL INVESTIGATOR: Shawn Hochman, PhD

CONTRACTING ORGANIZATION: Emory University, Atlanta, GA 30322

REPORT DATE: December 2018

TYPE OF REPORT: FINAL

PREPARED FOR: U.S. Army Medical Research and Materiel Command
Fort Detrick, Maryland 21702-5012

DISTRIBUTION STATEMENT: Approved for Public Release;
Distribution Unlimited

REPORT DOCUMENTATION PAGE

Form Approved
OMB No. 0704-0188

1. REPORT DATE
DECEMBER 2018

2. REPORT TYPE
Final

3. DATES COVERED
9/30/2014- 9/29/2018

4. TITLE AND SUBTITLE
Spinal Cord Injury-Induced Dysautonomia via Plasticity in Paravertebral Sympathetic Postganglionic

5a. CONTRACT NUMBER
W81XWH-14-1-0616

5b. GRANT NUMBER
SC130225

5c. PROGRAM ELEMENT NUMBER

6. AUTHOR(S)
Shawn Hochman, PhD

E-Mail: shochm2@emory.edu

5d. PROJECT NUMBER

5e. TASK NUMBER

5f. WORK UNIT NUMBER

7. PERFORMING ORGANIZATION NAME(S) AND ADDRESS(ES)

Emory University, 599 Clifton Road, 4
Atlanta, GA, 30322

8. PERFORMING ORGANIZATION REPORT NUMBER

9. SPONSORING / MONITORING AGENCY NAME(S) AND ADDRESS(ES)

U.S. Army Medical Research and Materiel Command
Fort Detrick, Maryland 21702-5012

10. SPONSOR/MONITOR'S ACRONYM(S)

11. SPONSOR/MONITOR'S REPORT NUMBER(S)

12. DISTRIBUTION / AVAILABILITY STATEMENT

Approved for Public Release; Distribution Unlimited

13. SUPPLEMENTARY NOTES

14. ABSTRACT

Sympathetic postganglionic neurons (**SPNs**) located in sympathetic ganglia represent the final common sympathetic motor output. Even though spinal cord injury (**SCI**) produces a profound plasticity in sympathetic autonomic function, the extent that SCI-induced dysautonomia is based on SPN changes within thoracic sympathetic ganglia is unknown. Given their strategic site in autonomic signaling to body, any plasticity is likely to be of high significance, yet there few studies due to their relative inaccessibility. We solved the accessibility problem then leveraged whole-cell recordings and transgenic approaches to study their function then dysfunction after SCI.

The two most significant findings during the funding period are:

(i) Whole-cell recordings reveal thoracic SPNs have a dramatically amplified excitability than previously thought, with greater intrinsic capacity for synaptic integration and with an ability for maintained firing to support sustained actions on vasomotor tone and thermoregulatory function.

(ii) Observed heterogeneity in responses of membrane and synaptic response properties after SCI is partly dependent on time after injury. SPNs are initially hypo-responsive with a trend toward becoming hyper-responsive after SCI.

15. SUBJECT TERMS
Spinal cord injury, autonomic dysreflexia, optogenetics, whole-cell patch clamp, sympathetic, autonomic, electrophysiology, plasticity, paravertebral, postganglionic

16. SECURITY CLASSIFICATION OF:			17. LIMITATION OF ABSTRACT	18. NUMBER OF PAGES	19a. NAME OF RESPONSIBLE PERSON
					USAMRMC
a. REPORT	b. ABSTRACT	c. THIS PAGE			19b. TELEPHONE NUMBER *(include area code)*
Unclassified	Unclassified	Unclassified	Unclassified	28	

Standard Form 298 (Rev. 8-98)
Prescribed by ANSI Std. Z39.18

Contents

The text of the report must include all sections addressed in the table of contents to include the following. **<u>DO</u>** include the bolded section headings, but **<u>DO NOT</u>** include the *italicized* descriptions of section contents in your submitted reports.

1. INTRODUCTION:

Sympathetic <u>post</u>ganglionic neurons (**SPNs**) located in sympathetic ganglia represent the final common sympathetic motor output. Even though SCI produces a profound plasticity in sympathetic autonomic function, the extent that SCI-induced dysautonomia is based on SPN changes within the thoracic paravertebral sympathetic chain is unknown. Given their strategic site in autonomic signaling to body, any plasticity is likely to be of high significance, yet there is a paucity of studies undoubtedly due to their near anatomical inaccessibility. We have solved the accessibility problem with a strategic methodological advance. We will determine the extent to which paravertebral SPNs are a nodal site for vasomotor dysfunction after SCI.

We will undertake physiological, pharmacological and optogenetic studies to examine network and cellular plasticity induced by SCI to answer the following two questions: (a) Does SCI lead to plasticity in synaptic interactions between preganglionics, SPNs and primary afferents? (b) Do SPNs become hyperresponsive to synaptic inputs after SCI?

2. KEYWORDS:

Spinal cord injury, autonomic dysreflexia, optogenetics, whole-cell patch clamp, sympathetic, autonomic, electrophysiology, plasticity, paravertebral, postganglionic

3. ACCOMPLISHMENTS:

The PI is reminded that the recipient organization is required to obtain prior written approval from the awarding agency Grants Officer whenever there are significant changes in the project or its direction.

a. What were the major goals of the project?

1. *List the major goals of the project as stated in the approved SOW. If the application listed milestones/target dates for important activities or phases of the project identify these dates and show actual completion dates or the percentage of completion.*

Characterizing thoracic chain sympathetic postganglionics		
Major Task 1a: Convergence and divergence	**months**	**% completion/ Completion dates**
Subtask 1: Segment specific properties	1-6	75%
Subtask 2: Pharmacology	7-12	*75%*
Subtask 3: Breeding/crossing transgenic mice and spinalizations	1-36	18months behind target
Subtask 3: Establish intracellular recording techniques	3-18	100%
Major Task 1b: Convergence and divergence	**months**	
Subtask 1: Incorporation of optogenetic approaches for selective activation of neuron populations	12-18	100%
Milestone(s) Achieved: Understanding of synaptic organization in uninjured mice and ability to use optogenetics to selectively activate afferent and efferent fiber populations		
Intracellular recordings and optogenetics		
Major Task 2: Characterize mechanisms responsible for dysautonomia after spinal cord injury using intracellular recordings and optogenetics	**months**	**% completion/ Completion dates**
Subtask 1: Physiological plasticity in preganglionic-postganglionic interactions assessed using optogenetics	18-36	40%
Subtask 2: Physiological plasticity in afferent-postganglionic interactions assessed using optogenetics	18-36	5%
Subtask 3: Physiological plasticity in preganglionic-afferent interactions assessed using optogenetics	18-36	0%
Subtask 4: Intracellular recordings of synaptic and cellular plasticity in membrane properties; demonstration of membrane bistability	18-36	50%
Milestone(s) Achieved: Demonstration of important contribution of thoracic sympathetic chain to SCI-induced autonomic plasticity and forward insight into therapeutic interventions for future study		
Data analysis and publications		
Major Task 3: Data analysis and publications	**months**	**% completion/ Completion dates**
Subtask 1: Data analysis	6-36	65%
Subtask 2: Manuscript writing and submission	24-36	55%
Milestone(s) Achieved: Dissemination of scientific results.		

b. What was accomplished under these goals?

major activities; 2) specific objectives; 3) significant results or key outcomes, including major findings, developments, or conclusions (both positive and negative)

Accomplishments under specific sections are described below followed by an overall annual summary that synthesizes these accomplishments. Please refer to figures in the overall summary as needed.

<u>1a.1: Segment specific properties</u>

<u>Methods/experiment</u>: Mice are euthanized (.2mL 50% urethane) and thoracolumbar spinal column quickly removed. The vertebral column is cut longitudinally, both dorsally and ventrally, and spinal roots are severed to remove spinal cord. Remaining vertebral column and ribs are trimmed to include only the thoracic region*. The tissue is pinned down in a Sylgaard recording chamber and suction electrodes are positioned to stimulate various thoracic ventral roots and record from various thoracic ganglia.

<u>Progress/results:</u> In the annual progress report in 2016 we used extracellular recordings to show that there is a convergence onto individual ganglia. For example, stimulating T4-T11 ventral roots results in activity in the T11 ganglion. The studies involved electrical stimulation of ventral roots and we proposed to repeat these trials using a genetic approaches for optical stimulation of ventral roots. The advantage here is that recruitment is likely in size principle order and that use of ChAT::CHR2 ensures that axonal recruitment from ventral roots is exclusively recruiting preganglionic cholinergic neurons and not inadvertently activating primary afferents that we showed previously and as has been reported also project visceral afferents through some ventral roots in thoracic segments. We have just begun assessment using optogenetics including after spinal cord injury.

<u>1a.2: Pharmacology</u>

<u>Methods/experiment</u>: Dissected vertebral column described in the methods section above is pinned down in recording chamber with stimulating suction electrodes on various ventral roots and a recording electrode on thoracic ganglia. We have been testing for synaptic transmitter identity by applying glutamatergic, cholinergic, nitrergic, purinergic and adrenergic ionotropic receptor antagonists to the recording chamber.

Progress/results:

Extracellular Recordings. We have found evidence for a contribution from glutamatergic, nitrergic and cholinergic transmission in both ventral root and dorsal root evoked responses. Postganglionic transmission is thought to occur via nicotinic acetylcholine receptor subunits. We have conducted experiments with nAChR antagonists that act on different receptor subunits and have found reduction from baseline synaptic transmission. We have increase sample size in the previous year and we've also broadened our pharmacological approach to include assessment of neuromodulation by sympathomimetics that include octopamine as well as β-phenylethylamine.

Intracellular Recordings. Experiments continue to assess the effects of various channel blockers on intrinsic membrane currents and synaptic events in intracellular recordings from individual neurons (**Figure 1**).

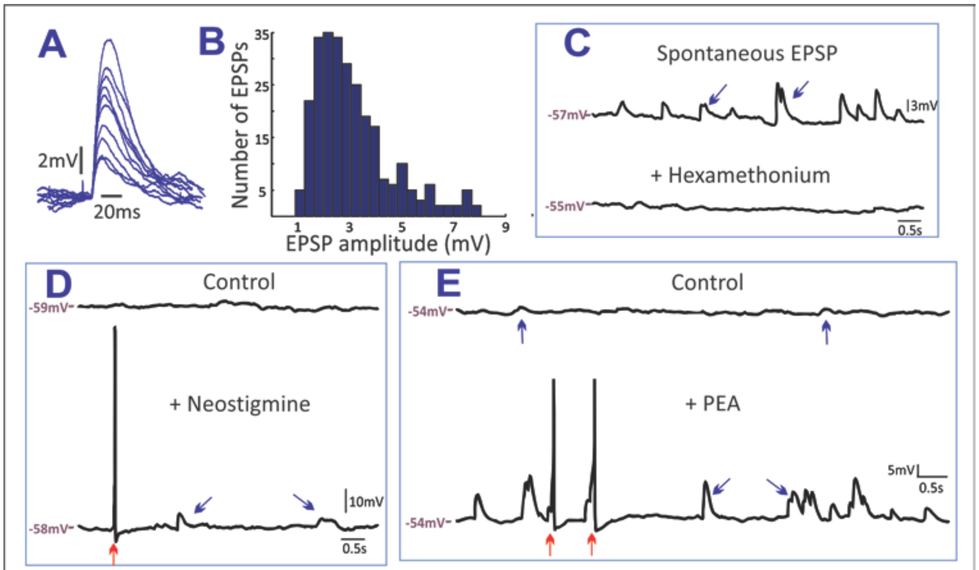

Figure 1. tSPN spontaneous EPSPs are cholinergic and modulated by PEA. A. Overlaid traces of captured EPSPs in one spontaneously active cell. **B.** Histogram of events showing that EPSP amplitudes occupy a continuous range from 1 to 8mV. C-D. Spontaneous EPSPs are cholinergic. They were blocked by 100uM hexamethonium (nAChR antagonist), and enhanced by 10uM neostigmine (acetylcholinesterase). E. 30uM PEA dramatically increased the amplitude and frequency of spontaneous EPSPs. Blue arrow: spontaneous EPSP. Red arrow: spontaneous EPSP triggered spike.

1a.3: Breeding/crossing transgenic mice and spinalizations
Methods/experiment: Standard animal husbandry
Progress/results: We currently have a healthy colony of ChAT-IRES-Cre::ChR2 mice available for performing in vitro optogenetic studies. We believe these mice will be more suitable than the BAC transgenics we previously used due to the more precise nature of their transgene insertion. These mice are used for all studies, with the exception of subtask 2.2. Subtask 2.2 will require the generation of Advillin::ChR2 mice to study afferent-postganglionic interactions. We are in possession of the requisite mouse strains, but have refrained from crossing them until other subtasks have neared completion.
As stated in the annual progress report in 2016, spinalizations are behind schedule. This has not changed. For example, in our last series of spinalizations with n=5, only one survived the requisite three week period we deemed necessary to examine plasticity at a time with known autonomic dysreflexia. Two animals were sacrificed early after spinalization (in the first week) due to health concerns. Two mice died from ruptured bladders due to manual expression even though individuals undertaking manual expression has significant experience, it appears that the bladder itself becomes more easily ruptured with manual expression pressures that previously were not sufficient to induce rupture. The difficulty of caring for injured mice compounded with the relatively low success rate of our intracellular recording technique has slowed progress in this area.
1a.4: Establish intracellular recording techniques
Methods/experiment: Starting with the preparation to isolate the thoracic chain and after ribs and vertebrae are trimmed (see 1a.1 methods, *) the entire tissue is incubated at 37°C in collagenase (and now dispase) for 1.5 hours. The tissue is then washed in physiological saline. Sympathetic chain is removed by severing rami and transferred to a recording chamber. Chain is pinned down in Sylgard, connective tissue is removed by scraping lightly with an insect pin, and recorded using standard patch clamp technique.
Progress/results: We now fully achieve acceptable recordings from most mice used in experiments, with recordings that can last > 1hour. These longer recordings are required to characterize convergent synaptic input properties and to study membrane current pharmacology. Progress overall has been steady, but still slower than we had hoped.

1b.1: Incorporation of optogenetic approaches for selective activation of neuron populations
Methods/experiment: We have developed a laser-diode based stimulator which allows for optical activation of preganglionic axons in ChAT::ChR2 mice. Light can be directed to illuminate ventral roots (primarily for extracellular recordings), interganglionic nerve, or thoracic ganglia.
Progress/results: Evoked synaptic response fatigues due to repeated stimulation, and takes seconds to recover. Details were described in the annual progress report for 2016. We have now begun to examine these evoked responses after SCI in the data has yet to be fully analyzed. Please refer back to last year's annual report for detailed observations.

2.1: Physiological plasticity in preganglionic-postganglionic interactions assessed using optogenetics
Methods/experiment: Methods described in 1b.1 are repeated in spinal cord injured mice.
Progress/results: Progress has been slow in this area. Tissue from injured mice appears to be more difficult to patch, i.e. high resistance seals are hard to achieve and recordings are "leaky." In light of this observation, we intend to stain the tissue for extracellular matrix components (collagen, chondroitin sulfate proteoglycans) to test the hypothesis that the extracellular matrix becomes denser after SCI. As stated previously, we have hired a new technician to help streamline the injury and recording process.

2.2: Physiological plasticity in afferent-postganglionic interactions assessed using optogenetics
Methods/experiment: &/ Progress/results: We have abandoned these experiments due to unanticipated difficulty in success rates and other experiments as well as difficulty in maintaining our Advillin-Cre breeding population.

2.3: Physiological plasticity in preganglionic-afferent interactions assessed using optogenetics
Methods/experiment: &/ Progress/results: We have abandoned these experiments due to unanticipated difficulty in success rates and other experiments as well as difficulty in maintaining our Advillin-Cre breeding population.

2.4: Intracellular recordings of synaptic and cellular plasticity in membrane properties; demonstration of membrane bistability
Methods/experiment:
Progress/results: SCI may induce greater frequency of spontaneous synaptic events. However, we currently have n=8, 3 of which are at early injury time, so this must be replicated before we can say this with confidence.

3.1: Data analysis
Methods/experiment: Data is analyzed in Clampfit, MATLAB, and/or Excel.
Progress/results: Basic cellular properties (input resistance, membrane capacitance, time constant, firing rate) have been analyzed. Analysis of synaptic properties are in progress.

3.2: Manuscript writing and submission

Table 1. Mean area and diameter values (±SD)				
	SCI (N = 7)	**Naive (N = 5)**	**P-Value**	**Power**
Mean Area	298±45	374±61	**0.02**	0.70
Mean Diameter	20.9±1.3	23.5±1.8	**0.015**	0.75
Mean Numbers	194±77	271±127	**0.10**	0.34

Methods/experiment: N/A
Progress/results: Manuscript writing is in progress. The abstract and methods and results sections are essentially complete. The results section is still in progress.

Further UPDATES.

(A) Characterization of cellular properties in adult mouse thoracic paravertebral ganglia.

By using whole-cell patch clamp recordings in intact thoracic ganglia, we have been able to record tSPNs in intact *ex vivo* thoracic ganglia to characterize their cellular and synaptic properties. We now have a trong dataset of 39 healthy cells is shown in Table 2 (mean values ± SD). Resting membrane potential, input resistance and membrane time constant (τ_m) were substantially higher than those reported in previous studies in the adult mouse (resting membrane potential is 10mV lower, input resistance is 9 times higher and τ_m is 13 times longer) (Jobling and Gibbins, 1999). Rheobase varied greatly between cells, but values were still approximately 10 times lower than those reported previously (Jobling and Gibbins, 1999). Threshold voltage was typically 18 mV higher than resting membrane potential, and action potentials displayed after-hyperpolarization. All neurons were capable of repetitive firing, in contrast to previous reports of only phasic firing with depolarizing current (Jobling and Gibbins, 1999). These differences are most likely due to the preservation of cell physiology with our whole-cell patch in contrast to the disruption of cell properties by impalement injury using sharp electrodes in previous studies. In our whole-cell patch, maximal firing rates observed in response to depolarizing current steps ranged from 14-17 spikes/sec. During intracellular depolarization, firing rate increased with increased current injection and cells sustained tonic firing. Spike frequency adaptation was also observed. All recorded properties are fully consistent with those reported recently with whole cell recordings in the rat superior cervical ganglia (Springer et al., 2015). We also observed a notable I_h current in 8 out of 13 cells. Its activation generally required hyperpolarization beyond -100mV and I_h current was more pronounced with greater hyperpolarization. With activation of I_h current, cells often displayed a post-inhibitory rebound spike, which may be a major factor contributing to oscillatory activity discussed below. We are also able to gauge the magnitude of A-type potassium currents (I_A). The current amplitude of I_A current amplitude following a hyperpolarization voltage step is comparable to reported study is comparable, but of much longer duration when compared to prior reports.

Table 2. *Summary of basic membrane properties*				
Property	Mean	±	SD	*n*
Membrane properties				
Resting membrane potential, mV	-58.8	±	7.2 (39)	39
Input Resistance, MΩ	1072	±	553 (38)	38
Membrane time constant, ms	94.3	±	54.8 (38)	38
Capacitance, pF	89.2	±	26.8 (38)	38
Threshold				
Absolute voltage, mV	-41.2	±	7.1 (39)	39
Relative to V_{hold}, mV	26.0	±	7.7 (39)	39
Rheobase, pA	27.5	±	16.0 (39)	39
Action Potential				
Amplitude, mV	55.0	±	15.7 (39)	39
Peak, mV	13.8	±	18.2 (39)	39
Half-width, ms	4.6	±	1.1 (39)	39
Rise slope, mv/ms	47.3	±	24.2 (39)	39
Afterhyperpolarization				
Amplitude, mV	15.1	±	3.7 (26)	26
Half-decay, ms	80.8	±	34.9 (26)	26
Duration, ms	230	±	71 (26)	26
F-I slope				
Max., Hz/pA	0.126	±	0.033 (39)	39
Sustained, Hz/pA	0.075	±	0.025 (39)	39

While a full manuscript for submission on these membrane properties was expected to be submitted by June, additional observations and incorporation of additional modeling has extended the process and we now anticipate a submission date of December 2017. The current version of the manuscript is attached

Comparing cellular properties after SCI.

Changes in connectivity following SCI may involve anatomical changes in tSPNs themselves. First, in the sparsely-labeled TH::TdTomato healthy animal, we observed very few dendrites in adrenergic neurons in caudal compared to rostral thoracic paravertebral ganglia (annual report 2016). This lack of dendrites in caudal ganglia is an important factor in considerations of tSPN excitability, including lack of persistent inward currents (**PICs**) and membrane bistability. In motoneurons, membrane bistability is associated with dendritic expression of PIC related voltage-gated channels. Thus anatomical changes such as increased dendritic arborization of tSPN will be consistent with the hypothesis that PICs emerge post-SCI.

Preliminary recordings suggest that I_A activation/inactivation dynamics may be lengthened after SCI (**Figure 2**). These preliminary studies of intrinsic cellular properties of unidentified tSPNs provide a demonstration of the power of whole patch recordings for discovery of tSPN physiology. With specific I targeting of NPY-positive vasoconstrictor tSPNs, I will be able to definitively determine intrinsic properties related to vasomotor function.

(B) Anatomical and synaptic plasticity after spinal cord injury.

Anatomical plasticity after spinal cord injury.

We have now compared counts and diameters of thoracic sympathetic postganglionic neurons from the T5 segment. Samples were in naïve controls (n=5) and mice having undergone spinal transection at thoracic level two (T2) three weeks prior (n=7). Adrenergic neurons were identified in whole ganglion immunohistochemical reaction for tyrosine hydroxylase (TH). Counts and size (area/diameter) of T5 neurons positive for TH were undertaken using Neurolucida software (MicroBrightField). We conducted t-tests with a significance level of α=0.05. We observed that after SCI, mean area and diameter of adrenergic neurons were statistically decreased (Table 1). We also compared average cell numbers, though there was a numerical 28% reduction in cell numbers after SCI, the observed significant variability and low sample size did not provide sufficient power to reliably determine statistical significance. Future plans are to increase our sample size as well as extend observations to other ganglia.

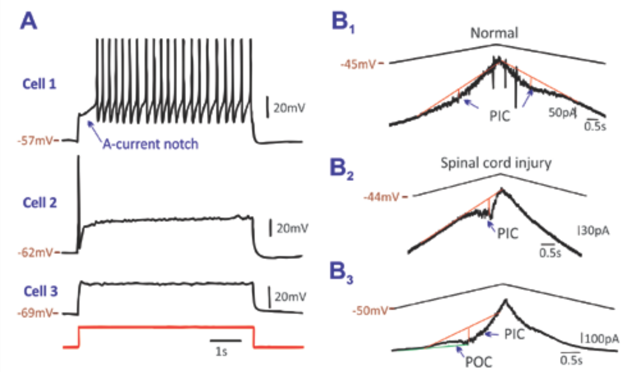

Figure 2. Weak firing but enhanced PICs at the acute stage after SCI (5 days post-SCI. A. Examples of three different firing property responses to same 100pA injected current (red trace). Cell 1 has similar firing frequency and amplitude compared to normal animals, but has a ~300ms long A current notch. Cell 2 only has a single spike, even with greater injected current. Cell 3 doesn't spike. **B.** Examples of persistent inward currents (PICs) before (**B_1**) and 5 days after injury (**B_2-B_3**). **B_1**. tSPN PICs from a naive animal. **B_2-B_3**. Acutely after SCI (5 days), larger PIC emerges. **B_2**. larger PIC in tSPN phasically spikes. **B_3**. In a neuron with repetitive firing, there is an emergence of initial persistent outward current (POC) followed by a larger PIC. Red vertical line: amplitude of PIC; Green vertical line: amplitude of POC.

Significant differences in cell area and diameter between SCI and naive T5 ganglia could be due to influence of sex rather than treatment. However, when we compared the average area and diameter of male versus females we saw no significant differences in mean areas or diameters. Within the constraints of our limited population size, we conclude that sex is not a factor.

Synaptic properties of paravertebral neurons.

The previous annual report (2016) provided details of our recordings of spontaneous and optogenetically evoked synaptic responses. This past year was associated with breeding issues that prevented us from undertaking various optogenetic stimulation experiments. Nonetheless we have had good success with increasing our success rate of whole cell recordings and this will enable a more complete assessment of ongoing spontaneous synaptic activity in the naïve preparation.

We have just begun to assemble data set of evoked responses in the spinal cord injured animals, but the data is too recent to provide quantitative analyses and is simply shown in figure that we believe is representative of observed differences (**Figure 3**).

We have also just begun to use an optogenetic approach to assess divergence of preganglionic axons arising from spinal segments onto individual thoracic chain ganglia onto individual tSPNs (*Fig X*). These results are also very recently obtained and preclude position of quantitative assessment at this stage.

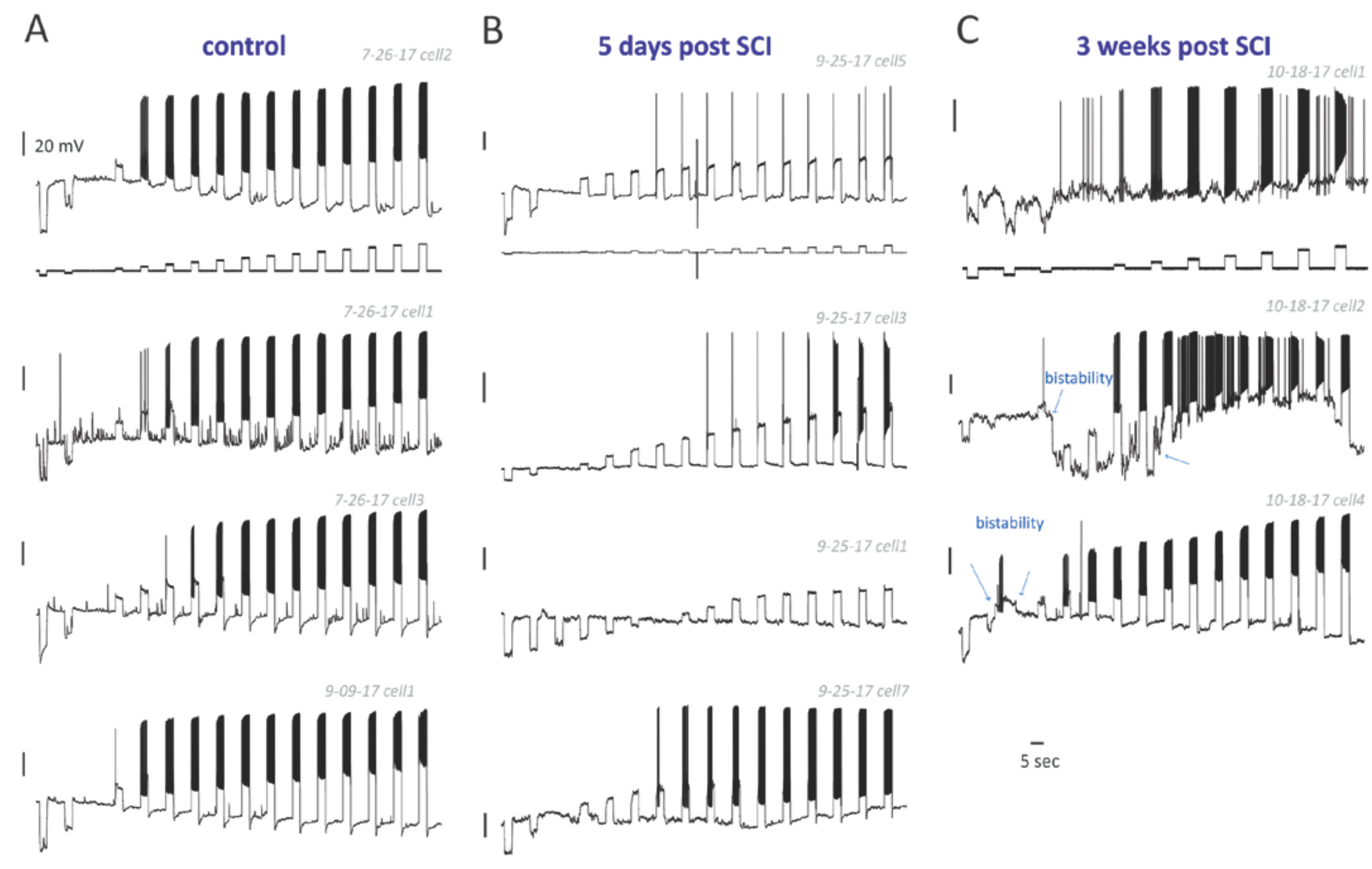

Figure 3. Comparison of firing properties in uninjured mice (A) and those having undergone T2 spinalization 5 days (B) or 3 weeks prior (C). **A.** Note that there is a sever reduction in excitability 5 days post-SCI (B) and that membrane potential instability including expression of shifts in membrane potential are notable 3 weeks post-SCI. Horizontal bar is 20 mV in all voltage recordings. Current step protocol is shown in upper row in all three panels.

4) other achievements.

Difficulty in obtaining recordings from spinal cord injured tissue.

We've had considerable difficulty in obtaining access to the cellular properties of these neurons after spinal cord injury. One possibility is that the injury leads to the generation of novel structural/cellular components that surround sympathetic ganglia. The working hard at trying to modify experimental approach and have begun to obtain success in the last month. This data has yet to be analyzed. Having said that recording quality has still been suboptimal and we have just ordered dispase as an additional protease to apply in conjunction with collagenase in an attempt to make the neuronal tissue more accessible.

We have found this to make an enormous difference and now have recordings from several neurons after spinal cord injury.

c. What opportunities for training and professional development has the project provided?

- *One individual was sent to a specialty meeting on spinal cord function in Marseille France to present his work and two individuals are being sent to the Annual Society for Neuroscience Meeting in San Diego this November.*
- *Three undergraduate students have worked on this project. Two of them I have worked on this model system in the last year, with one student undertaking a senior research project with poster present (attached).*

d. *Describe briefly what you plan to do during the next reporting period to accomplish the goals and objectives.*

- *We have received a no-cost extension, we plan to stay consistent with the major tasks outlined in the charts except for Major Task 2, subtasks 2 and 3.*
- *Regarding electrophysiology, emphasis will be on assessment of physiological plasticity*
- *Regarding anatomical assessment, we will continue towards the changed emphasis on more overtly describing the previously implicit neuroanatomical assessment of injury-induced plasticity using immunolabeling approaches.*
- *During this no-cost extension, a significant amount of time will be devoted to data analysis and manuscript writing.*

4. IMPACT:

- **What was the impact on the development of the principal discipline(s) of the project?**
  - *Result and disseminated information brought awareness to the importance of the sympathetic chain as a site capable of undergoing plasticity after SCI and therby likely contributing to the plethora of dysautonomias that are observed in individuals after SCI.*
- **What was the impact on other disciplines?**
  - *Led to a CRCNS application with a computational neuroscientist.*
  - *Led to a R01 application with a computational neuroscientist*
- **What was the impact on technology transfer?**
  - *Nothing to Report*
- **What was the impact on society beyond science and technology?**
  - *Derived insights may lead to a conceptual shift in current doctrine on therapeutic sites to target for clinical control of dysautonomia.*

5. CHANGES/PROBLEMS:

Please see above. We have a no-cost extension to try and complete some of the major goals of the grant.

6. PRODUCTS:

Nothing to Report

Publications, conference papers, and presentations
Other publications, conference papers, and presentations. *Identify any other publications, conference papers and/or presentations not reported above. Specify the status of the publication as noted above. List presentations made during the last year (international, national, local societies, military meetings, etc.). Use an asterisk (*) if presentation produced a manuscript.*

1. M. L. MCKINNON, S. HOCHMAN. Patch clamp recordings of cellular and synaptic properties in adult mouse thoracic paravertebral ganglia. Soc. Neurosci. Abst. 42 (2016).
2. Halder, M.C., M.; MacDowell, C.; McKinnon, M.; Sawchuk,M.; Hochman,S. (2016). Anatomy of mouse thoracic sympathetic chain ganglia and electrophysiological assessment of their multisegmental preganglionic input. Paper presented at: Society for Neuroscience.
3. Choi MHH (2015) Anatomical survey of paravertebral sympathetic chain in adult mice. In: Department of Neuroscience and Behavioral Biology: Emory.

4. LI, Y., M. L. MCKINNON, M. HALDER, S. HOCHMAN. Plasticity of thoracic sympathetic post-ganglionic neuron after spinal cord injury. Soc. Neurosci Abst 387.07 (2018).
5. TIAN, K., M. L. MCKINNON, S. HOCHMAN, A. A. PRINZ. Identifying cellular dynamics in mouse sympathetic neurons: A computational modeling approach. Soc. Neurosci Abst 387.02 (2018).
6.

7. PARTICIPANTS & OTHER COLLABORATING ORGANIZATIONS

What individuals have worked on the project?

- *Mallika Halder – 25% effort – research specialist*
- *Michal McKinnon – 90% effort – graduate student*
- *Michael Sawchuk, - 50% effort - lab manager*
- *Yaqing Li – 33% effort - postdoctoral fellow*
- *Lucy Galvin – 10% effort - Senior undergraduate research project*

e. Has there been a change in the active other support of the PD/PI(s) or senior/key personnel since the last reporting period?

- *P.I. NIH R01. Recruitment principles and injury-induced plasticity in thoracic paravertebral sympathetic postganglionic neurons. 6/2017-6/2022, $1,250,000 direct.*
- *PI. Craig H Neilsen Foundation. Continuous sensor-based home-cage recordings for SCI research. 10/16-10/19, $600,000 total.*
- *Co P.I. NIH R01. (NS102850). Examining the roles A-delta LTMRs and BDNF signaling play in neuropathic pain after SCI. 7/1/2018 – 6/30/23.*
- *Co P.I. NIH R21. Homeostatic plasticity in the homeostatic sympathetic nervous system. 4/2018-4/2020.*
- *P.I. PVA Research Foundation (#3166) Sleep dysfunction in spinal cord injury.1/2019-1/2021, $150,000 total.*

f. What other organizations were involved as partners?

- *Nothing to Report*

8. SPECIAL REPORTING REQUIREMENTS

9. APPENDICES:

g. paper submitted to e-Neuro

eNeuro

https://eneuro.msubmit.net

eN-TNWR-0433-18X

Dramatically amplified thoracic sympathetic postganglionic excitability and integrative capacity revealed with whole-cell patch clamp recordings

ABSTRACT

Thoracic paravertebral sympathetic chain postganglionic neurons (tSPNs) comprise the final integrative output of the distributed sympathetic nervous system controlling vascular and thermoregulatory systems. Considered a non-integrating relay, what little is known of tSPN intrinsic excitability has been determined by sharp microelectrodes with presumed impalement injury. We thus undertook the first electrophysiological characterization of tSPN cellular properties using whole-cell recordings and coupled results with a conductance-based model to explore the principles governing their excitability in adult mice of both sexes.

Recorded membrane resistance and time constant values were an order of magnitude greater than previously obtained leading to a demonstrable capacity for synaptic integration in driving recruitment. Variation in membrane resistivity was the primary determinant controlling cell excitability with resultant vastly lower currents required for tSPN recruitment. Unlike previous microelectrode recordings in mouse that observed inability for sustained firing, all tSPNs were instead capable of repetitive firing. Computational modeling demonstrated that observed differences are explained by introduction of a microelectrode impalement injury conductance. Overall, tSPNs largely linearly encoded injected current magnitudes over a broad frequency range with distinct subpopulations differentiable based on repetitive firing signatures.

Thus, whole-cell recordings reveal tSPNs have a dramatically amplified excitability than previously thought, with greater intrinsic capacity for synaptic integration and with an ability for maintained firing to support sustained actions on vasomotor tone and thermoregulatory function. Rather than acting as a relay, these studies support a more responsive role and possible intrinsic capacity for tSPNs to drive sympathetic autonomic function.

SIGNIFICANCE STATEMENT

Thoracic paravertebral sympathetic postganglionic neurons (tSPNs) represent the final neural output for control of vasomotor and thermoregulatory function. We used whole-cell recordings and computational modeling to provide broad insight on intrinsic cellular mechanisms controlling their excitability. Compared to past intracellular recordings using microelectrode impalement, we observed dramatically higher membrane resistivity with primacy in controlling enhanced tSPN excitability and recruitment via synaptic integration. Compared to reported phasic firing, all tSPNs fire repetitively and linearly encode injected current magnitude to firing frequency over a broad range. Modeling studies suggest that microelectrode impalement injury accounts for the differences in tSPN properties previously observed. Overall, intrinsic tSPN excitability plays a much greater role in the integration and maintenance of sympathetic output than previously thought.

INTRODUCTION

Sympathetic postganglionic neurons within paravertebral chain ganglia (SPNs) represent a large fraction of the final output of the sympathetic nervous system. Whereas prevertebral sympathetic ganglia are typically associated with one or more visceral organs in a discrete location (celiac ganglion, superior/inferior mesenteric ganglion), thoracic paravertebral chain ganglia are associated with control of dispersed tissue systems such as vasculature, brown adipose tissue, sweat glands, and piloerector muscles (Jänig, 2006; Bartness et al., 2010). As such, the sympathetic chain can be thought of as a distribution system for sympathetic activity that spans the body. The vast majority of paravertebral postganglionic neurons in mice are adrenergic (Gibbins, 1991; Jobling and Gibbins, 1999) since sweat glands, innervated by cholinergic postganglionic neurons, are largely absent in the mouse (Lu and Fuchs, 2014).

Traditionally, thoracic sympathetic postganglionic neurons (tSPNs) have been envisioned as passive followers of intraspinal preganglionic neuronal activity. By this viewpoint, postganglionic neurons fire if and only if preganglionics fire and serve as 1:1 relays that pass central commands to the periphery (Jänig, 2006). This relationship is explained by the "n+1" rule, wherein postganglionic neurons receive n small synaptic inputs, and one major, always suprathreshold input which leads to firing with a high safety factor. The n smaller synaptic inputs are typically sub-threshold and infrequent, and are not thought to contribute appreciably to the firing rate (McLachlan et al., 1998; Karila and Horn, 2000; McLachlan, 2003; Wheeler et al., 2004; Rimmer and Horn, 2010).

Despite their critical importance as the final output controlling sympathetic neural commands, surprisingly little is known about the SPNs in thoracic segments (tSPNs) of the sympathetic chain. The most likely reason for this is their near inaccessibility to in vivo study, and the relative difficulty for in vitro cellular characterization. The electrical properties of paravertebral sympathetic neurons are commonly studied in mammalian superior cervical ganglion (Eccles, 1935; Erulkar and Woodward, 1968; Purves and Wigston, 1983; Li and Horn, 2006) and to a lesser extent the stellate and lumbar ganglia (Jänig, 1985; Cassell et al., 1986; Valli et al., 1989; Bratton et al., 2010). Only a few studies have revealed electrophysiological properties of thoracic ganglia (Blackman and Purves, 1969; Lichtman et al., 1980; Jobling and Gibbins, 1999). These studies used sharp microelectrodes for recordings that likely introduce a considerable impalement injury conductance compared to whole-cell patch clamp recordings (Staley et al., 1992; Springer et al., 2015). This injury-induced conductance alters basic membrane properties, such as input resistance and membrane time constant, which reduce recruitment and synaptic integrative actions according to classical cable theory (Rall, 2011; Springer et al., 2015). Microelectrode impalement recordings that introduce an injury conductance can also prevent expression of repetitive firing properties (Cymbalyuk et al., 2002; Springer et al., 2015). Indeed, while it is generally thought that most paravertebral SPNs fire phasically (Cassell et al., 1986; Jobling and Gibbins, 1999; Li and Horn, 2006), whole-cell recordings in superior cervical ganglia support repetitive rather than phasic firing (Springer et al., 2015). Whether repetitive firing properties are predominant in tSPNs remains unknown.

The aim of the present study is to investigate the electrophysiological properties of tSPNs using whole cell recordings to more accurately characterize the cellular mechanisms that drive and modulate excitability of tSPNs. We furthermore matched recordings to a computational model to better understand how passive and active membrane properties interact to recruit neurons and generate the firing properties observed.

MATERIALS & METHODS

Animals

All animal procedures were performed in accordance with the [Author University] Institutional Animal Care and Use Committee's regulations and conformed to the Guide for the Care and Use of Laboratory Animals. Experiments were performed on adult (P37-379) C57BL/6 mice. Mice were anesthetized with inhaled isoflurane and maintained or killed with urethane (i.p. injection, 40mg/kg for transcardial perfusions, ~500mg/kg for *in vitro* electrophysiology). Complete sedation or death was confirmed by lack of foot pinch and eye blink reflex.

Immunohistochemistry

Neurotransmitter identity

Two ChAT-eGFP mice (JAX:007902), a male and a female (P91 and P101, respectively) were anesthetized and transcardially perfused with heparinized saline (0.9% NaCl, 0.1% $NaNO_2$, 10units/mL heparin), followed by 4% paraformaldehyde (0.5M phosphate, 4% paraformaldehyde, NaOH). Tissue was post-fixed overnight, then transferred to a 15% sucrose solution and stored at 4°C. Sympathetic chains were isolated from stellate (T1 and T2) to T12/13. Tissue was embedded (TissueTek® optimal cutting temperature compound), sectioned on a cryostat (−21°C, 8μm slice thickness), and mounted on glass slides. Tissue was washed in 0.1M phosphate buffered saline (PBS) for one hour and permeabilized with PBS containing 0.3% Triton X-100 (PBS-T) overnight. Sections were subsequently incubated for 2-3 days with primary antibodies: sheep anti-Tyrosine Hydroxylase (Millipore, 1:100) and chicken anti-green fluorescent protein (Jackson, 1:100). Preparations were then washed in PBS-T (3 x 30 min) and incubated for 1.5 hours with secondary antibodies: Cy3 donkey anti-sheep (Abcam, 1:250) and Alexa 488 donkey anti-chicken (Abcam, 1:250). Slides were washed a final time in PBS-T (20 min), then 50mM Tris-

HCl (2 x 20 min) and allowed to dry before being coverslipped (SlowFade® Gold antifade reagent with 4',6-diamidino-2-phenylindole (DAPI)). Sections were visualized under a fluorescent microscope (Olympus BX51). Cells with visible nuclei were counted and assessed for neurotransmitter identity. Inter-animal cell count variability was substantial (6,494 vs. 19,721 cells).

Cell diameter

Six C57Bl/6J mice (JAX: 000664), 5 males and one female (all ~P60) were transcardially perfused, as above. T5 Sympathetic ganglia were isolated. Unmounted tissue was washed in PBS-T overnight. Slides were subsequently incubated for 5 days with sheep anti-Tyrosine Hydroxylase (Millipore, 1:100). Preparations were then washed in PBS-T (3 x 2 hours) and incubated for 3 days with Alexa 488 donkey anti-sheep (Jackson, 1:100). Slides were washed a final time in PBS-T (2 hours), then 50mM Tris-HCl (2 x 1 hour). Intact ganglia were mounted on glass slides and coverslipped (SlowFade® Gold antifade reagent with DAPI). TH-immunoreactive cells were visualized under a fluorescent microscope (Olympus BX51, 40X objective) using a Microfire digital camera (Optronics, Santa Barbara, CA), and traced using Neurolucida software (MBF Bioscience, Burlington, VT). Cell diameters were calculated as the arithmetic mean of minimum and maximum feret. Diameter was only determined for cells with a discernible perimeter (176±131 cells per ganglion) representing a mean 71% of the total TH^+ cell population (range of 36-95% neurons/ganglia measured). As diameter distributions were comparable between ganglia, the possibility of sampling bias in estimated cell diameter is unlikely. Results are reported as mean ± SD.

Electrophysiology

Tissue Preparation

Mice were killed and the spinal column was quickly dissected out with sympathetic chain and spinal roots attached. Figure 1A provides a simplified schematic of the anatomic organization of intraspinal

preganglionic and paravertebral postganglionic neurons. The remaining tissue was incubated in continually oxygenated ACSF containing collagenase (20mg type III per 1mL ACSF, Worthington Biochemical Corporation) for 1.5 hours. ACSF used for incubation was buffered with either bicarbonate or HEPES. No difference was observed as a result of incubation buffer. Several incubations also included dispase type II (50mg in 1mL ACSF, Sigma Life Science). Following incubation, tissue was vortexed to remove adherent fat and washed with ACSF several times to eliminate residual collagenase. The intact sympathetic chain was removed by severing rami, and was then pinned down into a clear Sylgaard recording dish (Fig. 1B), through which recirculating, oxygenated ACSF was continually perfused.

Whole-cell recordings

Whole-cell patch recordings were obtained from postganglionic cells at room temperature. Cells were identified using an upright microscope (Olympus, BX51WI) affixed with a low-light camera (Olympus, OLY-150). Patch electrodes were pulled on a vertical puller (Narishige, PP-83) from 1.5mm outer diameter filamented, borosilicate glass capillaries (World Precision Instruments, stock # TW150F-4) for a target resistance of 5-9MOhms. Signals were amplified using a MultiClamp 700A and digitized at 10 kHz using a Digidata 1322A and Clampex software (Molecular Devices).

All recordings were made in ACSF containing (in mM): NaCl [127.99], KCl [1.90], $MgSO_4 \cdot 7H_2O$ [1.30], $CaCl_2 \cdot 2H_2O$ [2.40], KH_2PO_4 [1.20], glucose [9.99], and $NaHCO_3$ [26.04]. ACSF pH was adjusted to 7.4 after saturation with gas (95%O_2, 5%CO_2) at room temperature. Intracellular patch clamp solution contained (in mM): K-gluconate [140.0], EGTA [11.0], HEPES [10], and $CaCl_2$ [1.32] and pH was adjusted to 7.3 using KOH. Target osmolarity was less than 290 mOsm. In most recordings (25/39 cells), support solution was added consisting of ATP [4.0] and GTP [1.0].

preganglionic and paravertebral postganglionic neurons. The remaining tissue was incubated in continually oxygenated ACSF containing collagenase (20mg type III per 1mL ACSF, Worthington Biochemical Corporation) for 1.5 hours. ACSF used for incubation was buffered with either bicarbonate or HEPES. No difference was observed as a result of incubation buffer. Several incubations also included dispase type II (50mg in 1mL ACSF, Sigma Life Science). Following incubation, tissue was vortexed to remove adherent fat and washed with ACSF several times to eliminate residual collagenase. The intact sympathetic chain was removed by severing rami, and was then pinned down into a clear Sylgaard recording dish (Fig. 1B), through which recirculating, oxygenated ACSF was continually perfused.

Whole cell recordings

Whole-cell patch recordings were obtained from postganglionic cells at room temperature. Cells were identified using an upright microscope (Olympus, BX51WI) affixed with a low-light camera (Olympus, OLY-150). Patch electrodes were pulled on a vertical puller (Narishige, PP-83) from 1.5mm outer diameter filamented, borosilicate glass capillaries (World Precision Instruments, stock # TW150F-4) for a target resistance of 5-9MOhms. Signals were amplified using a MultiClamp 700A and digitized at 10 kHz using a Digidata 1322A and Clampex software (Molecular Devices).

All recordings were made in ACSF containing (in mM): NaCl [127.99], KCl [1.90], $MgSO_4 \cdot 7H_2O$ [1.30], $CaCl_2 \cdot 2H_2O$ [2.40], KH_2PO_4 [1.20], glucose [9.99], and $NaHCO_3$ [26.04]. ACSF pH was adjusted to 7.4 after saturation with gas (95% O_2, 5% CO_2) at room temperature. Intracellular patch clamp solution contained (in mM): K-gluconate [140.0], EGTA [11.0], HEPES [10], and $CaCl_2$ [1.32] and pH was adjusted to 7.3 using KOH. Target osmolarity was less than 290 mOsm. In most recordings (25/39 cells), support solution was added consisting of ATP [4.0] and GTP [1.0].

The ratio of male to female mice was approximately 1:1. Recordings were taken from the right thoracic ganglia, with the majority of recordings coming from T5. The number of cells from ganglia T3 through T12 was 4,7,18,3,2,1,1,0,1, and 2, respectively. No obvious differences were seen in recorded properties with respect to sex or thoracic level, so the data were pooled for population analysis. In all, we recorded from 39 cells whose resting membrane potentials were more negative than −45mV, and thus deemed of sufficient quality.

Data analysis

All cellular properties were analyzed in Clampfit (Molecular Devices) or MATLAB (MathWorks). All parameters were estimated from a single set of current steps for each cell. This ensured that parameters for a given cell were estimated at nearly the same point in time. In current clamp mode, membrane voltage response to hyperpolarizing current steps of at least 1.5 seconds was fit to an exponential of the form [1] using the Levenberg-Marquardt algorithm built in to Clampfit. The value of membrane time constant (τ_m) was calculated in this manner (Golowasch et al., 2009). R_{in} was estimated by dividing maximal voltage deflection (ΔV) by the injected current (I_{inj}) [2]. Membrane capacitance (C_m), a measure of total cell surface area, was estimated by dividing τ_m by R_{in} [3].

$$\Delta V \cdot \exp(-t/\tau_m) + V_{hold} \qquad [1]$$

$$R_{in} = \Delta V / I_{inj} \qquad [2]$$

$$C_m = \tau_m / R_{in} \qquad [3]$$

Rheobase current was taken as the smallest long-duration (1.5 seconds or longer) positive current injection which elicited a single spike. In the case that an incremental increase in current elicited multiple spikes, rheobase was estimated to be the mean of the adjacent subthreshold and

suprathreshold steps, *e.g.* if 30pA did not elicit any spikes but 40pA elicited several, the rheobase estimate would be 35pA.

Measured values related to action potential (AP) and post-spike afterhyperpolarization (AHP) characteristics were taken from traces elicited at rheobase current. The parameters of the fAHP varied as a function of firing rate, so analysis of fAHP properties was limited to cells which fired a single spike at rheobase intensity. Action potential threshold voltage was taken to be the point at which the first derivative of voltage, dV_m/dt, begins to increase at rheobase current injection (Platkiewicz and Brette, 2010). Action potential amplitude was defined as the difference between the peak voltage and threshold. AP half width is the width of the spike at half AP amplitude. Fast afterhyperpolarization (fAHP) amplitude was defined as the difference between peak negative voltage and steady-state voltage at rheobase current injection. fAHP half-decay is the time it takes for the fAHP to decay to half its amplitude. fAHP duration is the time between spike onset and return to baseline (Anonymous, 1994). Slow afterhyperpolarization (sAHP) amplitude was defined as the difference between peak negative voltage and baseline (holding voltage). sAHP half-decay is the time it takes for the sAHP to decay to half its amplitude.

Instantaneous firing rate (IFR) was taken as the inverse of the inter-spike interval. Maximal firing rate was the IFR for the first spike pair at the beginning of current onset. Sustained firing rate was the mean IFR for all subsequent spikes initiated during the depolarizing current step. The SRA ratio is defined as the ratio between the maximal and sustained firing rate at a given current injection (Venance and Glowinski, 2003; Miles et al., 2005). In order to directly compare firing rate across cells with variable R_{in} and *f*-I curves, we used the sustained firing rate at twice rheobase current injection. In cells which did not receive injection of twice rheobase (n=3), firing rate was estimated by interpolation or

extrapolation. Current step duration was at least 1.5 seconds for all cells, and 3 seconds for the majority. Liquid junction potential was calculated to be −9.8mV and empirically measured to be −13mV. All values of absolute voltage (resting membrane potential, absolute threshold, peak voltage) were adjusted by −10mV to approximately account for liquid junction potential.

Computational Modeling

Single Neuron Model

We built a conductance-based neuron model to help understand observed results in relation to their underlying biophysical mechanisms. While tSPNs do possess dendrites, their dendritic arborizations are relatively simple. We therefore assume that ganglionic cells are electrotonically compact, and that a single-compartment model can replicate all essential physiological properties observed in experiments. All currents included in the model have been observed in rodent sympathetic ganglia (Galvan and Sedlmeir, 1984; Sacchi et al., 1995; Jobling and Gibbins, 1999; Rittenhouse and Zigmond, 1999)

The model is based on a model of bullfrog paravertebral sympathetic ganglia (Wheeler et al., 2004), which represents the most complete available computational model of a paravertebral neuron. From this model the following conductances were taken: a fast sodium current, I_{Na}; a delayed-rectifier potassium current, I_{Kd}; a slow and non-inactivating potassium current, I_M; and a voltage-independent leak current, I_{leak}. Additional conductances were added from models derived in other species. These include the following: a fast transient potassium current, I_A (Rush and Rinzel, 1995); a hyperpolarization-activated inward current, I_h (Kullmann et al., 2016); and a calcium-dependent potassium current, I_{KCa} (Ermentrout and Terman, 2010). I_{KCa} depends on intracellular calcium concentration, $[Ca^{2+}]$, so a model of persistent calcium current, I_{CaL} (Bhalla and Bower, 1993) and somatic calcium dynamics (Kurian et al.,

2011) were added as well. Model parameters were then tuned to fit recorded data from the present study.

The membrane voltage, V, is updated according to the equation:

$$C_m \frac{dV}{dt} = -\sum I_i - I_{input} \qquad [4]$$

Membrane capacitance, C_m, was set at 100pF to approximate the mean in recorded neurons. Each current, I_i, is described by the equation:

$$I_i = G_i m^p h^q (V - E_i) \qquad [5]$$

where G_i is the maximal conductance, E_i is the reversal potential, and m and h are gating variables for activation and inactivation. A standard model neuron was used to replicate the majority of observed phenomena. This standard neuron has the following maximal conductances (in nS): G_{Na} is 300, G_{Kd} is 2000, G_{CaL} is 1.2, G_M is 50, G_{KCa} is 50, G_A is 50, G_h is 1, and G_{leak} is 1. This standard model was modified as necessary to fit individual recordings, which comprise a heterogeneous population.

The reversal potential is 60mV for I_{Na}; 120mV for I_{CaL}; −90mV for I_{Kd}, I_{KCa}, I_M, and I_A; −32mV for I_h; and −55mV for I_{leak}.

The activation and inactivation variables m and h are updated by the equation:

$$\frac{dx}{dt} = \frac{x_\infty - x}{\tau_x} \qquad [6]$$

The intracellular calcium concentration is updated by:

$$\frac{d}{dt}[Ca^{2+}] = \lambda(-\alpha I_{CaL} - k_{CaS}[Ca^{2+}]) \qquad [7]$$

where $\lambda = 0.01$ is the ratio of free to bound $[Ca^{2+}]$, $\alpha = 0.002$ uM·ms^{-1}·pA^{-1} is the conversion factor from current to concentration, and $k_{CaS} = 0.024$ ms^{-1} is the somatic $[Ca^{2+}]$ removal rate.

Impalement simulation

To replicate impalement injury, an additional leak conductance was added to the model in order to simulate microelectrode impalement. This conductance, g_{imp}, was modeled as a non-selective ohmic leak channel with $E_{imp} = -15$mV. The impalement reversal potential was estimated by solving the Goldman-Hodgkin-Katz equation, [8], with equal permeabilities of the three major ionic species. This estimate agrees well with estimates of impalement reversal potential in bullfrog ganglia (Brown, 1988). For analysis, model neurons were subjected to a bias current and held at −70mV.

$$E_m = \frac{RT}{F} ln\left(\frac{P_{Na}[Na^+]_{out} + P_K[K^+]_{out} + P_{Cl}[Cl^-]_{in}}{P_{Na}[Na^+]_{in} + P_K[K^+]_{in} + P_{Cl}[Cl^-]_{out}}\right) \qquad [8]$$

Code accessibility

Source code for all simulation and analysis are available in from the online repository [URL redacted for double-blind review] and ModelDB (Hines et al., 2004, accession # redacted). Simulation and analysis scripts were written in Python 2.7.10 and executed in PyCharm (CE 2017.1.2) on macOS 10.12.3 with a

1.7-GHz processor. Scripts were also translated into MATLAB code and executed on Windows 10 with a 2.4-GHz processor. All differential equations were integrated using an Exponential Euler method with a time step of 0.1 ms (Anonymous. et. al. 2004).

Experimental design and Statistical analysis

The present study used a descriptive design. Statistical analyses were performed in Microsoft Excel. Basic properties are presented as mean ± SD in Table 1. Correlations were determined by Pearson's correlation coefficient, r. A two-tailed t-test was used to calculate each p-value. To control for 29 multiple comparisons and maintain an experiment-wise α=0.05, a Šidák corrected α=0.0017 was used to assign statistical significance. In some cases, parameter pairs with moderate values of r, ($|r|$>0.4) failed to reach significance as a result of intrinsic variability inherent within this data. Such correlations are reported as moderate, and should be interpreted cautiously. Exact r, R^2, and p-values are presented in Table 2. Basic properties of tSPNs separated based on firing subtype were analyzed with a one-way ANOVA and Tukey's post hoc test, presented in Table 3. A p-value of less than 0.05 was considered significant.

RESULTS

1. Thoracic ganglia composition

Postganglionic neurons have been shown to be either adrenergic or cholinergic (Jobling and Gibbins, 1999; Jänig, 2006). In order to assess neurotransmitter identity throughout the sympathetic chain, we used a choline-acetyltransferase (ChAT) transgenic mouse which fluorescently labels putative cholinergic postganglionic neurons (ChAT::eGFP), and co-immunolabelled tissue with an antibody to tyrosine hydroxylase (TH) to label putative adrenergic neurons. Neurons were counted from stellate (T1 and T2) to T13 ganglia. We found that TH^+ neurons comprised >97% of the population and no ganglion contained greater than 6% presumptive cholinergic neurons. We therefore assume that the overwhelming majority of recorded cells were adrenergic.

As the majority of electrophysiological recordings focused on T5, diameter and number of TH-IR cells were examined in T5 ganglia in a separate sample from 6 adult mice (Fig. 1C). The mean number of TH-IR neurons counted in T5 ganglia was 247 ± 127 (ranging from 106-418). tSPNs had a mean cell diameter of 23.8 ± 5.4 µm with cell size distribution shown in Fig. 1D. These values are smaller than those reported previously (cf. Jobling and Gibbins, 1999).

2. Passive membrane properties

Whole cell patch clamp recordings were acquired from 39 tSPNs obtained from 33 adult mice. Basic cellular properties are summarized in Table 1. The distribution of resting membrane potential is shown in Fig. 2A. Input resistance (R_{in}) and membrane time constant (τ_m) were, on average, an order of magnitude higher than values recorded using microelectrode recordings in mouse (Jobling and Gibbins, 1999, see Fig. 2B) and guinea pig (Blackman and Purves, 1969) thoracic ganglia. R_{in} was strongly correlated with τ_m (Fig. 2B), but not cell capacitance (C_m), an estimate of cell size. This indicates that membrane resistivity, but not cell size, is primarily responsible for the variability seen in resistance measures (Gustafsson and Pinter, 1984). C_m was also moderately correlated with τ_m. A summary of correlation parameters is provided in Table 2.

One impact of larger τ_m is longer duration EPSPs and consequently greater capacity for temporal summation. Spontaneous synaptic activity is often observed in whole-cell recordings, including instances of EPSP summation that lead to recruitment of action potentials (Fig. 2C). In this neuron a τ_m of 109 ms led to comparably long EPSP membrane voltage decay τs.

3. Rheobase

The current required to depolarize a cell from its holding potential to firing threshold (rheobase) was examined in 39 cells by injecting long duration (1.5-3s) pulses through patch electrodes. In order to control for the possible influence of a variable resting membrane potential on rheobase, tonic bias current was injected to hold cells at approximately −70mV prior to rheobase estimation. Fluctuations in membrane voltage made it difficult to precisely set holding potential prior to injected current steps, and values ranged from −56 to −83 mV. We compared actual holding voltage against rheobase to determine if this variability altered rheobase estimation. Rheobase was not correlated with membrane potential.

Values of rheobase are presented in Table 1. The distribution of rheobase values can be seen on the abscissa in Fig. 3A. Rheobase values were 80-90% lower than values estimated in tSPNs previously with microelectrode recordings in both mouse and guinea pig (Blackman and Purves, 1969; Jobling and Gibbins, 1999). Reduced rheobase values indicate that tSPNs are much more excitable than previously considered. Rheobase current was strongly correlated with input conductance, $g_{in}=R_{in}^{-1}$ (Fig. 3A), and

moderately correlated with the inverse of time constant, τ_m^{-1}, but was uncorrelated with capacitance. A summary of correlation parameters is provided in Table 2.

We further investigated the relationship between input conductance and rheobase in a model cell (model properties are described in the Methods section). We adjusted g_{leak} in order to vary input conductance of a model neuron over most of the range observed in recorded neurons (0.5 to 3nS). Bias current was adjusted to hold the model cell at −70mV. The rheobase was then calculated for each value of input conductance by using a binary search algorithm to find the minimal injected current which produces a spike (Fig. 3A, gray line). The results show that there is a deterministic relationship between rheobase and input conductance that can help to explain some of the correlation observed in recorded neurons. However, given the variability of rheobase measures in recorded cells with comparable values for input conductance, it is clear that input conductance alone does not fully explain the range of rheobase values observed in recorded neurons.

Voltage threshold was assessed at rheobase current intensity. Assuming cell depolarization is governed by Ohmic or non-rectifying processes, the product of rheobase and input resistance would predict the voltage threshold (Gustafsson and Pinter, 1984). Indeed, the two values are well correlated (Fig. 3B, Table 2) and approximately equal, indicating that rectifying currents do not plat a major role in determining threshold voltage for the population. However, deviation of threshold values above and below those predicted by ohmic processes, support a role for from voltage-dependent conductances (Gustafsson and Pinter 1984).

4. Repetitive firing

Increasing current steps were delivered to assess repetitive firing properties from a holding potential of approximately −70mV. All cells (n=39) were capable of repetitive firing in response to sustained current injection. This contradicts an earlier report that tSPNs fire phasically in response to depolarization (Jobling and Gibbins, 1999). Fig. 4A shows an example of a recorded cell which fires repetitively at progressively higher frequency in response to increasing depolarizing current steps (top). A model neuron that used known voltage-dependent conductances for paravertebral sympathetic neurons (see Methods for a complete list) and incorporated values for input conductance obtained from our whole-cell recordings was able to replicate repetitive firing (Fig. 4A, bottom).

The discrepancy between observations of phasic and repetitive firing likely arises as a result of leak introduced by microelectrode impalement (Springer et al., 2015). We undertook additional modeling to test whether an impalement injury can convert repetitive to phasic firing. An additional impalement conductance, g_{imp}, was added to a standard model cell. Reversal potential of g_{imp} was set at −15mV. We explored the relationship between g_{imp} and firing type over a range of conductance and current injection combinations (Fig 4B). For a given set of g_{imp} and injected current, a cell could be non-firing (n), phasic firing (p), or repetitively firing (r). Setting g_{imp} to 7nS results in an input resistance of ~100MΩ, the mean value of input resistance reported by Jobling and Gibbins (1999). At this value, phasic firing was observed in response to suprathreshold current injection over the range of values tested by Jobling and Gibbins (1999). However, when g_{imp} was set at 0nS, analogous to a whole-cell recording, repetitive firing was observed instead (Fig 4Bi). The boundaries between firing types were identified using a binary search algorithm. There is a rapid transition from repetitive to phasic firing as g_{imp} is increased.

Prior studies have reported that phasic firing sympathetic neurons could fire repetitively if I_M was blocked (Brown and Adams, 1980; Cassell et al., 1986). To test this, we blocked I_M in our model cell by setting g_M to 0nS. This change completely eliminated phasic firing in the model, and only repetitive firing was observed (Fig. 4Bii). g_{imp} was only included for this figure, and all subsequent references to leak conductance refer to physiological leak, g_{leak}.

Frequency-current (*f*-I) relations were obtained by plotting the maximal (initial) and sustained firing rate versus injected current magnitude. Fig. 4Ci and 4Cii show the maximal and sustained (respectively) *f*-I curves for all cells. Maximal instantaneous firing rate did not exceed 28 Hz, while sustained firing rate did not exceed 17 Hz for the highest steps given. Maximal *f*-I curves were approximately linear and sustained *f*-I curves were concave down. In order to determine the role that input conductance plays in determining *f*-I relations in tSPNs, we selected a model neuron that matches the experimental mean *f*-I curves and then systematically varied input conductance over a range that covers the majority of experimentally-obtained values (0.7 to 3 nS). Of note, varying input conductance also changes holding potential so in order to remain consistent with experimental protocol, each model neuron was subjected to a different holding current to hold the initial voltage at −70mV. Fig. 4Ciii and 4Civ demonstrates that changing input conductance by altering g_{leak} can shift the *f*-I curve, but *f*-I curves for experimental values occupied a much wider range. Thus, input conductance cannot fully account for the range of firing frequencies seen.

Slope for both maximal and sustained *f*-I curves was calculated as a measure of excitability (Anonymous, 2010). In short, a cell with a higher *f*-I slope would respond to an incremental change in current with a higher change in firing frequency. In this way, *f*-I slope can be thought of as the gain between input and output of a neuron. Values for maximal and sustained *f*-I slope are given in Table 1.

We assessed the role of variations in R_{in} and rheobase in cell excitability based on ƒ-I slope measures. Firing rate at 100pA current injection was moderately correlated with R_{in}. ƒ-I slope was moderately correlated with R_{in} (Fig. 4D). ƒ-I slope was also negatively correlated with rheobase (Fig. 4E). No such relationship was found for τ_m or C_m. A summary of correlation parameters is provided in Table 2. Cells with lower rheobase and higher R_{in} had higher ƒ-I slopes, suggesting that Ohmic properties help govern the frequency-current response.

5. Spike rate adaptation

Implicit in the observation that sustained firing rates were lower than initial observed frequencies is that all cells displayed spike rate adaptation (SRA), or a decrease in firing rate over time. We were able to replicate SRA in our model (Fig. 5A). The time-course of adaptation consists of a fast and a slow phase (Fig. 5B).

The difference between the initial firing rate and the sustained firing rate becomes more pronounced as injected current is increased in all cells. This can be illustrated by comparing the maximal ƒ-I curve to the sustained ƒ-I curve in both recorded and model neuron over a range of current injection (Fig. 5C). This relationship between maximal and sustained firing rate is a common feature of adapting neurons (Benda and Herz, 2003).

Several mechanisms have been proposed to underlie SRA in different neuronal populations including Na^+ channel inactivation (Miles et al., 2005), fast AHP summation (Powers et al., 1999), activation of I_{KCa} (Miles et al., 2005) and activation of I_M (Yi et al., 2015). We selectively removed conductances from the model and determined which were primarily responsible for SRA (Fig 5D). Removal of I_{KCa} preferentially

impaired the later phase of adaptation (curve 1) while removal of I_M preferentially impaired the early phase of adaptation (curve 2). Removal of both I_{KCa} and I_M completely eliminated SRA (curve 3). Our model supports the conclusion that the combination of these conductances is necessary in order to replicate SRA.

6. Cell firing type classification

We noted variability in spike height of the initial spike compared to subsequent spikes in a spike train during repetitive firing. Neurons were divided into three categories based on the peak voltage of the initial spike in a spike train compared to the peak voltage of subsequent spikes. Of the 39 neurons examined, the initial spike had slightly lower amplitude than subsequent spikes in 22 cells (type 1), and substantially higher amplitude in 13 cells (type 2) (Fig. 6A). In type 1 and 2 cells, this phenomenon became more pronounced with greater current injection. In 4 cells, both firing patterns were observed, with type 1 characteristics at lower current steps giving way to type 2 characteristics at higher current steps (type 3). The difference between the initial spike peak voltage and the mean spike peak voltage was plotted for all cells as a function of calculated change in membrane voltage (injected current x R_{in}) (Fig. 6B). These differences did not appear to be associated with any basic membrane properties, threshold properties or the fAHP (defined below). In contrast, all measured parameters related to action potential (AP) shape showed significant difference between groups including maximal rise slope (Fig. 6C), peak value (Fig. 6D) (one-way ANOVA). All AP parameters differed significantly between type 1 and type 2 cells. A summary of statistical measures is given in Table 3. However, as a post hoc power analysis indicated a power of 0.5, we cannot conclusively say that there are no other significant differences between groups.

7. Afterhyperpolarization

Afterhyperpolarization (AHP) dynamics play an important role in regulating neuronal firing. Based on decay time, we identified three types of AHP within the thoracic ganglia. These include the fast AHP (fAHP) after a single action potential, and the slow AHP (sAHP) and ultra-slow AHP (usAHP) after a several action potentials (Fig. 7A).

Fast post-spike after-hyperpolarization (fAHP) amplitude, half-decay time, and duration were measured at rheobase current injection (Fig. 7A i). Parameters related to fAHP are summarized in Table 1. Half-decay time was very well correlated with duration and more reliably obtained, so further analysis focused on fAHP half-decay time. fAHP half-decay time was compared to passive membrane properties and rheobase. fAHP half-decay time was not correlated with R_{in} or C_m, but was moderately correlated with τ_m and negatively and moderately correlated with rheobase (Fig. 7B). Previous studies have reported an inverse relationship between fAHP duration and firing rate in motoneurons (Brownstone et al., 1992; Stauffer et al., 2007). To determine if this relationship exists in postganglionic neurons, we plotted fAHP half-decay time versus sustained firing rate at twice rheobase current injection. We found that there is indeed a strong negative correlation between fAHP half-decay time and maximal firing rate at twice rheobase (Fig. 7C). fAHP half-decay time was also moderately correlated with sustained ƒ-I slope but not maximal ƒ-I slope.

Slow AHPs (sAHP) were also observed following larger depolarizing steps that elicited higher repetitive firing frequencies (Fig. 7A ii). Only cells displaying obvious sAHP were analyzed (n=30 of 39). sAHPs were measured at maximal current injection. Parameters related to sAHP are summarized in Table 1. sAHP half-decay time was four-fold longer on average than fAHP half-decay, but the two were not correlated. To examine the relationship between sAHP and SRA, we plotted the sAHP half-decay versus the SRA

ratio for 28 cells (Fig. 7D). We found the two parameters were moderately correlated. A summary of correlation parameters for both fAHP and sAHP is provided in Table 2. As with SRA, our computational model showed that I_M and I_{KCa} were capable of reproducing sAHP after repetitive firing (not shown).

Prior work in the rabbit superior cervical ganglion identified a long-lasting AHP following sustained depolarization that was due to the ouabain sensitive Na^+/K^+-ATPase (Lees and Wallis, 1974). In the neonatal mouse spinal cord, it has been shown to be due to activation of α3 Na^+/K^+-ATPase (Picton et al., 2017).This AHP is unique in its ability to hyperpolarize a cell membrane beyond the reversal potential of K^+. We identified an AHP with a similar time-course in mouse tSPNs, evidenced by a steadily increasing hyperpolarization in response to injected current (Fig. 7A iii). This feature was present in 3 of 18 cells tested with a current step protocol that would allow for its observation. Of note, the usAHP was observed only in relatively high resistance cells when ATP and GTP were included in the electrode solution. This AHP was also able to achieve a membrane potential of 101.7 ± 11.5 mV, which includes measures below the calculated −98 mV K^+ reversal potential (Fig. 7A iv). The time-course of this hyperpolarization is too long to be due to I_M or I_{KCa}.

8. Subthreshold conductances

Subthreshold conductances can play an important role in determining cell excitability and firing properties. We evaluated activation of these conductances with current steps that included assessment at hyperpolarized membrane potentials seen during the usAHP.

In response to depolarizing current steps, membrane voltage first followed an exponential time-course with subsequent recruitment of voltage-gated conductances that altered the trajectory. In 28 of 39 cells, membrane trajectory exhibited a negative deflection from the exponential trajectory which preceded activation of voltage gated Na^+ conductance. The observed deflection, or "notch", in membrane led to a delay in the first action potential in a train (Fig. 8Ci) and has been described previously in tSPNs (Jobling and Gibbins, 1999). This phenomenon was often observed at a holding potential of −70mV, and became more pronounced with greater hyperpolarization (−90mV). This is consistent with activation of the transient, voltage-gated A-type K^+ current (I_A). To test the contribution of I_A to the notch and delayed firing, we held a model neuron at two different holding potentials and found that the change in trajectory was indeed attributable to de-inactivation of I_A (Fig. 8Cii) (Rush and Rinzel, 1995). Notably, a similar notch was observed in cells displaying usAHP (Fig. 7Aiv), demonstrating that the usAHP leads to a state of membrane hyperpolarization where I_A would delay onset of firing.

During hyperpolarizing current injection, a depolarizing voltage "sag" was often observed. When present, a voltage sag was easily detected with membrane hyperpolarization beyond −100mV (Fig. 8Ai) but was also observed at less negative hyperpolarization (Fig. 8Bi). We found a voltage sag in 19 of 32 cells hyperpolarized to at least −100mV from a holding potential of −70mV. This phenomenon has been previously reported in mouse tSPNs (Jobling and Gibbins, 1999) and other mammalian sympathetic neurons (Cassell et al., 1986) where it has been attributed to the anomalous rectifier, or H-current (I_H). To support a role for I_H, this conductance was implemented in the computational model and was found to reproduce the observed voltage sag (Fig. 8Aii). I_H has also been shown to contribute to a more depolarized membrane potential (Pape, 1996; Lamas, 1998), so we compared resting membrane potential in cells with (n=19) and without (n=13) evidence of I_H but found no significant differences (Student's t-test, two-tailed, p=.16).

I_H has also been implicated in post-inhibitory rebound firing (Pape, 1996; Ascoli et al., 2010; Engbers et al., 2011; Ferrante et al., 2017). Sag was seen in 12 of 13 tSPNs exhibiting rebound firing, but rebound

firing was only observed when cells were held closer to firing threshold (between −60 and −50mV; Fig. Bi) where I_M has been shown to be responsible for inducing a voltage sag and rebound firing (Constanti and Galvan, 1983). We used a computational model to understand the relative contributions of I_H and I_M and determined that sag is due to I_H for significant hyperpolarizations, and I_M for more moderate hyperpolarization. Rebound firing can occur in the absence of I_H but does not occur in the absence of I_M following release from moderate (~10mV) hyperpolarization, indicating that I_H is neither necessary nor sufficient to induce rebound firing in tSPNs (Fig. Bii).

DISCUSSION

Re-appraisal of physiological consequence of passive membrane properties

We obtained the first whole-cell recordings of mouse tSPNs and built the first computational model to provide mechanistic insight into their function. Whole-cell recordings preserve membrane properties and provide an accurate representation of tSPN function. This is critically important, as the impalement conductance introduced by microelectrode recordings can change passive membrane properties (Staley et al., 1992; Cymbalyuk et al., 2002; Springer et al., 2015), reduce apparent excitability, underestimate the importance of synaptic convergence (Karila and Horn, 2000; Horn and Kullmann, 2007), and prevent repetitive firing (Springer et al., 2015).

Input resistance (R_{in}) and membrane time constant (τ_m) were highly correlated and their values, as well as rheobase, occupy an approximately ten-fold range. Values of R_{in} and τ_m are an order of magnitude larger than values previously obtained from the same population using traditional microelectrode recordings (Blackman and Purves, 1969; Jobling and Gibbins, 1999), which indicates that the excitability of tSPNs has been substantially underestimated. Measured cell diameters in the T5 ganglion occupied a five-fold range (cf. Jobling and Gibbins, 1999). Capacitance (C_m) values occupied a three-fold range, and were unrelated to cell recruitment. The strong observed relationship between R_{in} and measures of firing threshold (*i.e.*, rheobase) demonstrate that ohmic processes dominate tSPN recruitment. These observations suggest that membrane resistivity rather than cell size is the primary determinant of recruitment threshold across the population (Gustafsson and Pinter, 1984), though it is unclear if the observed variability in excitability represents a population recruitment principle.

The preservation of the passive membrane electrical properties R_{in} and τ_m leads to synaptic events of greater amplitude and longer duration, which has important consequences for synaptic recruitment.

Paravertebral neurons receive nicotinic EPSPs comprising both sub- and suprathreshold events of variable amplitude (Nishi and Koketsu, 1960; Blackman and Purves, 1969; Karila and Horn, 2000; Bratton et al., 2010). An overall increase in EPSP amplitude would convert many subthreshold events into suprathreshold events, thereby increasing tSPN firing rate (Bratton et al., 2010). Traditionally, summation of EPSPs was not thought to contribute to cell recruitment in paravertebral ganglia (North, 1986; McLachlan et al., 1997; Jänig, 2006). However, recent whole-cell recordings from rat superior cervical ganglion demonstrate long-duration EPSPs with much greater capacity for summation (Springer et al., 2015). We also observed long-duration EPSPs with decay time-constant comparable to τ_m and examples of EPSP summation leading to cell recruitment. This provides direct support for the gain hypothesis for amplification of preganglionic activity (Karila and Horn, 2000; Horn and Kullmann, 2007). The observed τ_m values indicate that tSPNs could act as integrators during states of strong preganglionic sympathetic drive from individual neurons (see Jänig, 1985; Ivanov and Purves, 1989) and could widen the temporal window for coincidence detection and summation of convergent synchronous preganglionic inputs (Skok, 1973; Konig et al., 1996; Ratte et al., 2013). These observations support the concept that tSPNs do not merely relay preganglionic activity, but rather actively integrate and amplify sympathetic output. Metabotropic receptor-mediated changes in intrinsic membrane conductances may further amplify this process (North, 1986; Karila and Horn, 2000).

Additionally important was the observation that all tSPNs were capable of firing repetitively. Three distinct populations were identified based on differences in properties of spike amplitude trajectory during repetitive firing. Measures of Na^+ channel availability such as maximal rise slope and amplitude of action potentials (Hodgkin and Huxley, 1952; Miles et al., 2005) predicted whether spike amplitude would increase or decrease over time. It is unclear if these populations correspond to known molecularly or functionally distinct subpopulations (Jänig, 1988; Gibbins, 1991; Jobling and Gibbins, 1999; Li and Horn, 2006; Furlan et al., 2016).

The observation of repetitive firing contrasts traditional observations in all paravertebral neurons, including tSPNs, of phasic firing in response to sustained current injection (Jobling and Gibbins, 1999; Jänig, 2006; Springer et al., 2015). Recent whole-cell recordings in rat SCG similarly found paravertebral neurons were capable of repetitive firing, and suggested the discrepancy was a result of impalement conductance (Springer et al., 2015). We were able to replicate these results using our model; by introducing an impalement conductance consistent with microelectrode impalement, we were able to convert repetitively firing model neurons to phasically firing model neurons. Phasic firing after impalement injury appears to be dependent on the presence of I_M, as blocking I_M can convert sympathetic neurons from phasic to repetitively firing (Brown and Adams, 1980; Brown and Constanti, 1980; Cassell et al., 1986; Luther and Birren, 2009). This observation was reproduced by subtracting I_M in our model. I_{KCa} has also been shown to contribute to the interconversion of sympathetic neuron membrane firing properties (Sacchi et al., 1995; Luther and Birren, 2009). Thus, the firing properties of paravertebral sympathetic neurons that exhibit I_M and I_{KCa} are particularly sensitive to impalement leak, which underscores the importance of using whole-cell recordings. Blackman and colleagues were able to observe repetitive firing with microelectrodes, a finding that has been consistently overlooked (Blackman and Purves, 1969). A possible explanation could be differences in ion channel expression between the mouse and guinea pig.

The physiological relevance of repetitive firing in tSPNs

The physiological relevance of repetitive firing in tSPNs in response to current stimulation might be dismissed if one assumes that postganglionic neurons are only driven by nicotinic preganglionic input.

However, paravertebral neurons can exhibit long-lasting depolarization and sustained firing (Blackman and Purves, 1969; Janig et al., 1982; Kawatani et al., 1987). Activation of metabotropic muscarinic and various other non-cholinergic receptors are implicated (Janig et al., 1982; North, 1986; Kawatani et al., 1987; Elfvin et al., 1993). These studies support the idea that tSPNs can generate sustained sympathetic drive with limited influence from preganglionics.

Passive membrane properties and various conductances are responsible for sculpting the firing response of tSPNs. R_{in} is important in determining firing rate over a range of injected current values. R_{in} also impacts the slope of the f-I curve. tSPNs with steeper slope may be more effective at amplifying postganglionic output gain (Salinas and Thier, 2000; Anonymous, 2010). Given the relatively low steady-state firing rates of preganglionic neurons observed *in vivo* (Jänig, 2006), the physiological relevance of variability in response amplification is unclear (Springer et al., 2015).

However, synaptic drive may contribute to response amplification during bouts of metabotropic receptor-mediated sustained activity described above. We observe spontaneous excitatory post-synaptic currents with amplitudes ranging from 10pA to over 100pA (data not shown). Comparing these amplitudes to values of rheobase (range 5-70 pA) supports conditions where synaptic actions are capable of transient response amplification.

Relating observed cellular properties to underlying conductances

While the firing rate of tSPNs is strongly determined by the temporal dynamics of the fAHP, a feature carried by I_A and I_K in rodent SCG (Belluzzi and Sacchi, 1988), the mechanisms underlying spike rate adaptation (SRA) have not been studied in paravertebral ganglia including tSPNs. SRA has been well characterized elsewhere (Benda and Herz, 2003; Benda and Tabak, 2013). Contributions from I_M and I_{KCa} are among the proposed mechanisms (Sawczuk et al., 1997; Powers et al., 1999; Miles et al., 2005; Yi et

al., 2015), and these currents have been previously identified in rodent paravertebral ganglia (Sacchi et al., 1995; Davies et al., 1996; Haley et al., 2000; Locknar et al., 2004; Maingret et al., 2008). Our modeling found that I_M and I_{KCa} were required to replicate the fast and slow components of SRA, respectively. I_M and I_{KCa} are also known to contribute to the slow AHP in rodent SCG and hippocampus (Storm, 1990; Sacchi et al., 1995), and inclusion of I_{KCa} or I_M in the model reproduced the sAHP after repetitive firing. That SRA ratio and sAHP half-decay were correlated further supports co-involvement of these conductances.

Other factors contributing to modulation of tSPN excitability

tSPNs are known to express I_A, I_H and I_M (Jobling and Gibbins, 1999). These currents have been shown to modulate EPSP amplitude, synaptic integration, membrane potential, and repetitive firing rate (Connor and Stevens, 1971; Storm, 1990; Rush and Rinzel, 1995; Hoffman et al., 1997; Lamas, 1998; Prescott et al., 2006; George et al., 2009; Kullmann et al., 2016). We found evidence of I_A, I_H and I_M in our recordings by observing phenomena such as notch, sag, and rebound firing, and we replicated their effects using computational modeling. These phenomena typically require hyperpolarization to emerge. While there are no known inhibitory synapses in sympathetic ganglia (McLachlan, 2007), a slow IPSP due to metabotropic activation of K^+ conductances has been observed in SCG (Libet and Kobayashi, 1974; North, 1986). Another method of hyperpolarization observed in a small group of tSPNs is the slowly developing usAHP that follows prolonged activity (Zhang and Sillar, 2012). The usAHP has been observed in rabbit SCG (Lees and Wallis, 1974) and reflects Na^+ dependent activation of the ouabain-sensitive α3 Na^+/K^+-ATPase (Picton et al., 2017). These long-lasting hyperpolarizations may provide a physiological mechanism by which the aforementioned phenomena may emerge.

REFERENCES

Ascoli GA, Gasparini S, Medinilla V, Migliore M (2010) Local control of postinhibitory rebound spiking in CA1 pyramidal neuron dendrites. J Neurosci 30:6434-6442.

Bartness TJ, Vaughan CH, Song CK (2010) Sympathetic and sensory innervation of brown adipose tissue. Int J Obes (Lond) 34 Suppl 1:S36-42.

Belluzzi O, Sacchi O (1988) The interactions between potassium and sodium currents in generating action potentials in the rat sympathetic neurone. J Physiol 397:127-147.

Benda J, Herz AV (2003) A universal model for spike-frequency adaptation. Neural Comput 15:2523-2564.

Benda J, Tabak J (2013) Spike-Frequency Adaptation. In: Encyclopedia of Computational Neuroscience (Jaeger D, Jung R, eds), pp 1-12. New York, NY: Springer New York.

Bhalla US, Bower JM (1993) Exploring parameter space in detailed single neuron models: simulations of the mitral and granule cells of the olfactory bulb. J Neurophysiol 69:1948-1965.

Blackman JG, Purves RD (1969) Intracellular recordings from ganglia of the thoracic sympathetic chain of the guinea-pig. The Journal of physiology 203:173–198.

Bratton B, Davies P, Jänig W, McAllen R (2010) Ganglionic transmission in a vasomotor pathway studied *in vivo*: Vasomotor ganglionic transmission *in vivo*. The Journal of Physiology 588:1647-1659.

Brown DA (1988) M Currents. In: Ion Channels (Narahashi T, ed), pp 55-94.

Brown DA, Adams PR (1980) Muscarinic suppression of a novel voltage-sensitive K+ current in a vertebrate neurone. Nature 283:673-676.

Brown DA, Constanti A (1980) Intracellular observations on the effects of muscarinic agonists on rat sympathetic neurones. Br J Pharmacol 70:593-608.

Brownstone RM, Jordan LM, Kriellaars DJ, Noga BR, Shefchyk SJ (1992) On the regulation of repetitive firing in lumbar motoneurones during fictive locomotion in the cat. Exp Brain Res 90:441-455.

Cassell JF, Clark AL, McLachlan EM (1986) Characteristics of phasic and tonic sympathetic ganglion cells of the guinea-pig. J Physiol 372:457-483.

Connor JA, Stevens CF (1971) Prediction of repetitive firing behaviour from voltage clamp data on an isolated neurone soma. J Physiol 213:31-53.

Constanti A, Galvan M (1983) M-current in voltage-clamped olfactory cortex neurones. Neurosci Lett 39:65-70.

Cymbalyuk GS, Gaudry Q, Masino MA, Calabrese RL (2002) Bursting in leech heart interneurons: cell-autonomous and network-based mechanisms. J Neurosci 22:10580-10592.

Davies PJ, Ireland DR, McLachlan EM (1996) Sources of Ca2+ for different Ca(2+)-activated K+ conductances in neurones of the rat superior cervical ganglion. J Physiol 495 (Pt 2):353-366.

Eccles JC (1935) The action potential of the superior cervical ganglion. The Journal of physiology 85:179–206.

Elfvin L-G, Lindh B, Hökfelt T (1993) The chemical neuroanatomy of sympathetic ganglia. Annual review of neuroscience 16:471–507.

Engbers JD, Anderson D, Tadayonnejad R, Mehaffey WH, Molineux ML, Turner RW (2011) Distinct roles for I(T) and I(H) in controlling the frequency and timing of rebound spike responses. J Physiol 589:5391-5413.

Ermentrout GB, Terman DH (2010) Mathematical Foundations of Neuroscience.

Erulkar SD, Woodward JK (1968) Intracellular recording from mammalian superior cervical ganglion in situ. J Physiol 199:189-203.

Ferrante M, Shay CF, Tsuno Y, William Chapman G, Hasselmo ME (2017) Post-Inhibitory Rebound Spikes in Rat Medial Entorhinal Layer II/III Principal Cells: In Vivo, In Vitro, and Computational Modeling Characterization. Cereb Cortex 27:2111-2125.

Furlan A, La Manno G, Lubke M, Haring M, Abdo H, Hochgerner H, Kuperi J, Usoskin D, Airaksinen MS, Oliver G, Linnarsson S, Ernfors P (2016) Visceral motor neuron diversity delineates a cellular basis for nipple- and pilo-erection muscle control. Nat Neurosci 19:1331-1340.

Galvan M, Sedlmeir C (1984) Outward currents in voltage-clamped rat sympathetic neurones. J Physiol 356:115-133.

George MS, Abbott LF, Siegelbaum SA (2009) HCN hyperpolarization-activated cation channels inhibit EPSPs by interactions with M-type K(+) channels. Nat Neurosci 12:577-584.

Gibbins IL (1991) Vasomotor, pilomotor and secretomotor neurons distinguished by size and neuropeptide content in superior cervical ganglia of mice. J Auton Nerv Syst 34:171-183.

Golowasch J, Thomas G, Taylor AL, Patel A, Pineda A, Khalil C, Nadim F (2009) Membrane capacitance measurements revisited: dependence of capacitance value on measurement method in nonisopotential neurons. J Neurophysiol 102:2161-2175.

Gustafsson B, Pinter MJ (1984) An investigation of threshold properties among cat spinal alpha-motoneurones. The Journal of Physiology 357:453.

Haley JE, Delmas P, Offermanns S, Abogadie FC, Simon MI, Buckley NJ, Brown DA (2000) Muscarinic inhibition of calcium current and M current in Galpha q-deficient mice. J Neurosci 20:3973-3979.

Hines ML, Morse T, Migliore M, Carnevale NT, Shepherd GM (2004) ModelDB: A Database to Support Computational Neuroscience. J Comput Neurosci 17:7-11.

Hodgkin AL, Huxley AF (1952) A quantitative description of membrane current and its application to conduction and excitation in nerve. J Physiol 117:500-544.

Hoffman DA, Magee JC, Colbert CM, Johnston D (1997) K+ channel regulation of signal propagation in dendrites of hippocampal pyramidal neurons. Nature 387:869-875.

Horn JP, Kullmann PHM (2007) Dynamic clamp analysis of synaptic integration in sympathetic ganglia. Neurophysiology 39:423-429.

Ivanov A, Purves D (1989) Ongoing electrical activity of superior cervical ganglion cells in mammals of different size. J Comp Neurol 284:398-404.

Janig W, Krauspe R, Wiedersatz G (1982) Transmission of impulses from pre- to postganglionic vasoconstrictor and sudomotor neurons. J Auton Nerv Syst 6:95-106.

Jänig W (1985) Organization of the lumbar sympathetic outflow to skeletal muscle and skin of the cat hindlimb and tail. In: Reviews of Physiology, Biochemistry and Pharmacology, Volume 102, pp 119-213. Berlin, Heidelberg: Springer Berlin Heidelberg.

Jänig W (1988) Pre- and postganglionic vasoconstrictor neurons: differentiation, types, and discharge properties. Annu Rev Physiol 50:525-539.

Jänig W (2006) The Integrative Action of the Autonomic Nervous System: Cambridge University Press.

Jobling P, Gibbins IL (1999) Electrophysiological and morphological diversity of mouse sympathetic neurons. Journal of neurophysiology 82:2747–2764.

Karila P, Horn JP (2000) Secondary nicotinic synapses on sympathetic B neurons and their putative role in ganglionic amplification of activity. The Journal of Neuroscience 20:908–918.

Kawatani M, Rutigliano MJ, de Groat WC (1987) Vasoactive intestinal polypeptide facilitates the late component of the 5-hydroxytryptamine-induced discharge in the cat superior cervical ganglion. Neurosci Lett 73:59-64.

Konig P, Engel AK, Singer W (1996) Integrator or coincidence detector? The role of the cortical neuron revisited. Trends Neurosci 19:130-137.

Kullmann PH, Sikora KM, Clark KL, Arduini I, Springer MG, Horn JP (2016) HCN hyperpolarization-activated cation channels strengthen virtual nicotinic EPSPs and thereby elevate synaptic amplification in rat sympathetic neurons. J Neurophysiol 116:438-447.

Kurian M, Crook SM, Jung R (2011) Motoneuron model of self-sustained firing after spinal cord injury. J Comput Neurosci 31:625-645.

Lamas JA (1998) A hyperpolarization-activated cation current (Ih) contributes to resting membrane potential in rat superior cervical sympathetic neurones. Pflugers Arch 436:429-435.

Lees GM, Wallis DI (1974) Hyperpolarization of rabbit superior cervical ganglion cells due to activity of an electrogenic sodium pump. Br J Pharmacol 50:79-93.

Li C, Horn JP (2006) Physiological classification of sympathetic neurons in the rat superior cervical ganglion. J Neurophysiol 95:187-195.

Libet B, Kobayashi H (1974) Adrenergic mediation of slow inhibitory postsynaptic potential in sympathetic ganglia of the frog. J Neurophysiol 37:805-814.

Lichtman JW, Purves D, Yip JW (1980) Innervation of sympathetic neurones in the guinea-pig thoracic chain. The Journal of physiology 298:285–299.

Locknar SA, Barstow KL, Tompkins JD, Merriam LA, Parsons RL (2004) Calcium-induced calcium release regulates action potential generation in guinea-pig sympathetic neurones. J Physiol 555:627-635.

Lu C, Fuchs E (2014) Sweat gland progenitors in development, homeostasis, and wound repair. Cold Spring Harb Perspect Med 4.

Luther JA, Birren SJ (2009) p75 and TrkA signaling regulates sympathetic neuronal firing patterns via differential modulation of voltage-gated currents. J Neurosci 29:5411-5424.

Maingret F, Coste B, Hao J, Giamarchi A, Allen D, Crest M, Litchfield DW, Adelman JP, Delmas P (2008) Neurotransmitter modulation of small-conductance Ca2+-activated K+ channels by regulation of Ca2+ gating. Neuron 59:439-449.

McLachlan EM (2003) Transmission of signals through sympathetic ganglia–modulation, integration or simply distribution? Acta Physiol Scand 177:227-235.

McLachlan EM (2007) Diversity of sympathetic vasoconstrictor pathways and their plasticity after spinal cord injury. Clinical Autonomic Research 17:6-12.

McLachlan EM, Davies PJ, Habler HJ, Jamieson J (1997) On-going and reflex synaptic events in rat superior cervical ganglion cells. J Physiol 501 (Pt 1):165-181.

McLachlan EM, Habler HJ, Jamieson J, Davies PJ (1998) Analysis of the periodicity of synaptic events in neurones in the superior cervical ganglion of anaesthetized rats. J Physiol 511 (Pt 2):461-478.

Miles GB, Dai Y, Brownstone RM (2005) Mechanisms underlying the early phase of spike frequency adaptation in mouse spinal motoneurones: Mechanisms underlying SFA in spinal motoneurones. The Journal of Physiology 566:519-532.

Nishi S, Koketsu K (1960) Electrical properties and activities of single sympathetic neurons in frogs. J Cell Comp Physiol 55:15-30.

North RA (1986) Mechanisms of Autonomic Integration. In: Compr Physiol 2011, Supplement 4: Handbook of Physiology, The Nervous System, Intrinsic Regulatory Systems of the Brain, pp 115-153.

Pape H C (1996) Queer current and pacemaker: The Hyperpolarization-Activated Cation Current in Neurons. Annual Reviews Physiology 58:299-327.

Picton LD, Nascimento F, Broadhead MJ, Sillar KT, Miles GB (2017) Sodium Pumps Mediate Activity-Dependent Changes in Mammalian Motor Networks. J Neurosci 37:906-921.

Platkiewicz J, Brette R (2010) A threshold equation for action potential initiation. PLoS Comput Biol 6:e1000850.

Powers RK, Sawczuk A, Musick JR, Binder MD (1999) Multiple mechanisms of spike-frequency adaptation in motoneurones. The Journal of Physiology 93:101-114.

Prescott SA, Ratte S, De Koninck Y, Sejnowski TJ (2006) Nonlinear interaction between shunting and adaptation controls a switch between integration and coincidence detection in pyramidal neurons. J Neurosci 26:9084-9097.

Purves D, Wigston DJ (1983) Neural units in the superior cervical ganglion of the guinea-pig. J Physiol 334:169-176.

Rall W (2011) Core Conductor Theory and Cable Properties of Neurons. In: Handbook of Physiology, The Nervous System, Cellular Biology of Neurons, pp 39-97.

Ratte S, Hong S, De Schutter E, Prescott SA (2013) Impact of neuronal properties on network coding: roles of spike initiation dynamics and robust synchrony transfer. Neuron 78:758-772.

Rimmer K, Horn JP (2010) Weak and straddling secondary nicotinic synapses can drive firing in rat sympathetic neurons and thereby contribute to ganglionic amplification. Front Neurol 1:130.

Rittenhouse AR, Zigmond RE (1999) Role of N- and L-type calcium channels in depolarization-induced activation of tyrosine hydroxylase and release of norepinephrine by sympathetic cell bodies and nerve terminals. J Neurobiol 40:137-148.

Rush ME, Rinzel J (1995) The potassium A-current, low firing rates and rebound excitation in Hodgkin-Huxley models. Bulletin of mathematical biology 57:899–929.

Sacchi O, Rossi ML, Canella R (1995) The slow Ca(2+)-activated K+ current, IAHP, in the rat sympathetic neurone. J Physiol 483 (Pt 1):15-27.

Salinas E, Thier P (2000) Gain modulation: a major computational principle of the central nervous system. Neuron 27:15-21.

Sawczuk A, Powers RK, Binder MD (1997) Contribution of outward currents to spike-frequency adaptation in hypoglossal motoneurons of the rat. J Neurophysiol 78:2246-2253.

Skok VI (1973) Physiology of autonomic ganglia. Tokyo: Igaku Shoin.

Springer MG, Kullmann PHM, Horn JP (2015) Virtual leak channels modulate firing dynamics and synaptic integration in rat sympathetic neurons: Implications for ganglionic transmission *in vivo*: Firing dynamics and synaptic gain in rat sympathetic neurons. The Journal of Physiology 593:803-823.

Staley KJ, Otis TS, Mody I (1992) Membrane properties of dentate gyrus granule cells: comparison of sharp microelectrode and whole-cell recordings. J Neurophysiol 67:1346-1358.

Stauffer EK, McDonagh JC, Hornby TG, Reinking RM, Stuart DG (2007) Historical reflections on the afterhyperpolarization--firing rate relation of vertebrate spinal neurons. J Comp Physiol A Neuroethol Sens Neural Behav Physiol 193:145-158.

Storm JF (1990) Potassium currents in hippocampal pyramidal cells. Prog Brain Res 83:161-187.

Valli P, Zucca G, Botta L, Seghezzi R (1989) Lumbar sympathetic ganglia in man: an electrophysiological study in vitro. J Auton Nerv Syst 28:211-217.

Vervance L, Glowinski J (2003) Heterogeneity of spike frequency adaptation among medium spiny neurones from the rat striatum. Neuroscience 122:77-92.

Wheeler DW, Kullmann PH, Horn JP (2004) Estimating use-dependent synaptic gain in autonomic ganglia by computational simulation and dynamic-clamp analysis. J Neurophysiol 92:2659-2671.

Yi G, Wang J, Tsang KM, Wei X, Deng B, Han C (2015) Spike-frequency adaptation of a two-compartment neuron modulated by extracellular electric fields. Biol Cybern 109:287-306.

Zhang HY, Sillar KT (2012) Short-term memory of motor network performance via activity-dependent potentiation of Na+/K+ pump function. Curr Biol 22:526-531.

FIGURE LEGENDS

Figure 1: Cell size and composition.

A, Simplified schematic depicting the anatomical organization of preganglionic and postganglionic neurons. ***B***, Recording setup. Sympathetic chains are pinned down in a silicone chamber, superfused with oxygenated ACSF. They are then visualized under a microscope and recorded using a glass patch-clamp electrode. ***C***, Confocal slice through whole-mounted tissue showing TH immunolabeling and nuclear labeling with DAPI. Note the numerous smaller and more intensely labeled nuclei that are presumably non-neuronal cells. Scale bar represents 50μm. ***D***, Histogram showing distribution of TH-IR cell diameters in T5 ganglia of 6 animals.

Figure 2: Passive membrane properties.

A, Histogram showing distribution of resting membrane potential values. ***B***, Input resistance is highly correlated with membrane time constant. Solid line indicates linear least-squares fit. Filled black circle represents population mean. Red filled circle, population mean from (Jobling and Gibbins, 1999). ***C***, Example of synaptic summation leading to action potential recruitment in a particularly active recording. Shown is a raster of epochs of spontaneous synaptic activity. Cell resting membrane potential was −60 mV. In this neuron a τ_m of 109 ms led to comparably long EPSP membrane voltage decay τs. Vertical scale bar is 20mV; horizontal scale bar is 500ms.

Figure 3: Factors affecting rheobase.

A, Rheobase was well correlated with input conductance in recorded neurons, open circles. Gray line represents the rheobase versus input conductance relationship for a single model neuron chosen to fit experimental data. Standard model cell with G_A=15nS. ***B***, There is a strong correlation between measured voltage threshold and the product of rheobase and R_{in}, suggesting that variations in R_{in}

account for differences in threshold excitability. Rheobase "voltage" is approximately equal to threshold voltage. Dashed line is line of identity. In both panels, solid line represents least squares regression.

Figure 4: tSPNs exhibit repetitive firing.

A, Top, representative trace from a tSPN showing increases in repetitive firing frequency in response to increasing current steps. Bottom, model neuron also showing repetitive firing. Standard model with G_M=30, G_{KCa}=70, G_A=80, G_{leak}=2nS. Injected current from left to right in both recorded neuron and model is 30, 50, 70, 90, 110, 130pA. Scale bar is 1s. ***B***, Impact of injected current and impalement conductance, g_{imp}, on firing type. (i) Solid lines denote the boundaries between non-firing (n), phasic firing (p), and repetitive firing (r). Open circles indicate the combined g_{imp} and injected current values used to generate inset traces. At g_{imp}=0nS, analogous to whole-cell recordings, the model neuron transitions rapidly from n to r, and repetitive firing results from any current injection above ~20pA. At g_{imp} = 7nS, analogous to microelectrode impalement injury, the model neuron transitions from n to p at around 200pA current injection, and repetitive firing is not observed for injected current less than 500pA. (ii) Removing I_M from the model by setting g_M=0nS eliminates phasic firing altogether, i.e., cells transition directly from n to r regardless of impalement conductance. Standard model with G_{leak}=0.5nS. ***C***, *f*-I relations for recorded and model neurons. (i) maximal instantaneous firing rate is plotted versus injected current for all cells. (ii), same as Ci with sustained firing rate. (iii) maximal *f*-I curve from a model neuron in which g_{leak} was adjusted to generate input conductances of approximately 0.5, 1, 2, and 3 nS. Note: as varying input conductance also changes holding potential, each model neuron was subjected to a different holding current to hold the initial voltage at -70mV. Also note that g_{leak} is distinct from g_{imp}. (iv) corresponding sustained *f*-I curves. Standard model with G_M=30nS, G_H=0nS. ***D***, Maximal *f*-I slope is positively correlated with input resistance. ***E***, Maximal *f*-I slope is negatively correlated with rheobase.

Figure 5: Modeling suggests that spike rate adaptation (SRA) in tSPNs depends on both I_M and I_{KCa}.

A, (i) Representative trace showing tSPN response to 50pA current injection. Note that the inter-spike interval increases over time, corresponding to a decrease in instantaneous frequency. (ii) Trace from a model cell chosen to fit the recording shows similar SRA for 50pA current injection. Maximal conductances are (in nS): G_{Na}=400, G_K=3000, G_{CaL}=1.2, G_M=40, G_{KCa}=60, G_A=80, G_H=1, G_{leak}=2. Scale bar in both panels is 1 second. ***B***, Instantaneous frequency versus time for the same recorded cell at 50, 70, 90, 110, 130pA current injection (from bottom to top). The 50pA curve (red) corresponds to the trace in panel Ai. Fast and slow components of adaptation are indicated. ***C***, Maximal and sustained f-I curves match well between recorded and modeled cell over a range of injected currents. Red, maximal (top, solid) and sustained (bottom, dashed) *f*-I curves for the cell in panel Ai and B. Blue lines are the corresponding *f*-I curves from the model cell in panel Aii. ***D***, Instantaneous frequency versus time curves for the model cell in panel Aii. The recorded 50pA curve from panel B is reproduced for comparison to the analogous curve generated in the model cell in Aii (blue). Black curves numbered 1-3 represent effect of removal of two conductances from the model. Removal of g_{KCa} (curve 1) predominantly influences the slow SRA. Removal of g_M (curve 2) predominantly influences the fast SRA. Removal of both (curve 3) eliminates SRA. The ordinate axis is shared among panels B-D.

Figure 6: tSPNs are differentiable into subtypes based on direction of spike height changes.

A, Example traces from a type 1 (left, black) and type 2 (right, blue) cell. Scale bar 200ms. ***B***, Population of cells showing a variety of firing types. The difference in the initial spike peak versus the mean of all subsequent spike peaks is plotted versus the product of injected current and input resistance for all cells (n=39). Type 1 cells with a positive change in spike peak are shown in solid black line; Type 2 cells with a negative change in spike peak are shown in dotted blue line; Type 3 cells which convert from type 1 to type 2 dynamics as injected current is increased are shown in dashed red line. *C*, Maximal rise slope for

all three cell types. Type 2 cells have a significantly higher rate of depolarization than type 1 and 3 (P=.001; P=.04 respectively). ***D***, Amplitude of the initial spike at rheobase current injection. Type 2 cells have significantly higher peak values than type 1 but not type 3 (P=.001; P=.09 respectively). Horizontal bars indicate mean value for C and D.

Figure 7: Afterhyperpolarization.

A, Side by side comparison of three types of AHPs. (i) fAHP present after single spike. (ii) sAHP is present in the same cell only after repetitive firing. The half-decay time of fast and slow AHPs are indicated by the gray bar beneath each trace. Scale bar 1s. (iii) Depolarizing current steps (10 to 130pA in 10pA increments) in a different cell showing the progressive hyperpolarization characteristic of the usAHP. Scale bar 10s. (iv) Expanded view of voltage traces in Aiii indicated by vertical arrows. Note that the gray trace is hyperpolarized by 20mV compared to the black trace and has a characteristic "notch" (arrowhead) upon depolarization. ***B***, AHP half-decay was negatively correlated with rheobase (R^2=.27). ***C***, AHP half-decay was negatively correlated with maximal firing rate at twice rheobase (R^2=.48). ***D***, SRA ratio is positively correlated with sAHP half-decay (R^2=.27, n=28). Black line is the linear fit.

Figure 8: Subthreshold conductances.

A, (i) Voltage "sag," indicated by arrow, upon hyperpolarization beyond -90mV in a cell held at -70mV. Note that the effect becomes more pronounced with greater hyperpolarization. (ii) Model neuron showing similar sag. Standard model with G_A=5 and G_{leak}=.1nS. ***B***, (i) Hyperpolarizing trace from a different cell held at -50mV showing rebound spiking associated with voltage sag. (ii) Model neuron showing rebound spiking at the same holding voltage and current injection. Maximal conductances are (in nS): G_{Na}=200, G_K=2000, G_{CaL}=1.2, G_M=20, G_{KCa}=20, G_A=20, G_H=1, G_{leak}=2. Removal of g_H (curve 1) does not inhibit rebound firing. Removal of g_M eliminates firing (curve 2) as does removal of both currents

(curve 3). ***C***, (i) A cell depolarized from -90 mV exhibits a characteristic notch (arrow) accompanied by a delay in spiking (black trace). The same cell depolarized from -70mV does not have a notch (gray trace). (ii) Model neuron showing comparable results with pre-spike inflection seen only for hyperpolarized trace. Standard model with G_M=10, G_{KCa}=10, G_A=90, G_{leak}=0nS. Inset: Magnitude of h_A at onset of current injection shows that I_A is less inactivated (h_A is higher) at hyperpolarized voltage, and I_A takes longer to fully inactivate. Scale bars represent 500ms for all panels.

TABLE LEGENDS

Table 1: Basic properties of tSPNs.

Values of basic properties of tSPNs reported as mean ± SD and range of observed values.

Table 2: Selected correlations between tSPN parameters

Selected correlations reported in results. *r*, Pearson's correlation coefficient. R^2, coefficient of determination. n, number of observations. p-values calculated from two-tailed t-test. Asterisk indicates statistically significant correlation at Šidák-corrected α<0.0017. R_{in}, input resistance; τ_m, membrane time constant; C_m, membrane capacitance; I_{Rheo}, rheobase current; V_{hold}, holding voltage; g_{in}, input conductance; V_{th}, threshold voltage; f_{max}, maximal instantaneous firing rate; f_{sus}, sustained firing rate; fAHP, fast afterhyperpolarization; sAHP, slow afterhyperpolarization.

Table 3: Comparison of basic properties of neuron subtypes

Values given as mean ± SD with number of observations in parentheses. [a,b]Statistically different groups as determined by one-way ANOVA and Tukey's post hoc test. RMP, resting membrane potential; R_{in}, input resistance; τ_m, membrane time constant; C_m, membrane capacitance; fAHP, afterhyperpolarization.

EXTENDED DATA LEGENDS

Extended Data 1: Computational model code

Python and MATLAB code for the computational model of tSPN. Documentation is provided within the code.

TABLES

Property	mean ± SD (n)	range
Membrane properties		
Resting membrane potential, mV	−58.8 ± 7.2 (39)	-46 to -80
Input Resistance, MΩ	1072 ± 553 (38)	246 to 2297
Input conductance, nS	1.25 ± 0.8 (38)	0.44 to 4.1
Membrane time constant, ms	94.3 ± 54.8 (38)	19 to 234
Capacitance, pF	89.2 ± 26.8 (38)	51 to 157
Threshold		
Absolute voltage, mV	-41.2 ± 7.1 (39)	-21.6 to -58.8
Relative to V_{hold}, mV	26.0 ± 7.7 (39)	11.8 to 46.6
Rheobase, pA	27.2 ± 15.9 (39)	5 to 70
Action Potential		
Amplitude, mV	55.0 ± 15.7 (39)	23.4 to 92.1
Peak, mV	13.8 ± 18.2 (39)	-30.8 to 48.2
Half-width, ms	4.6 ± 1.1 (39)	2.9 to 7.8
Rise slope, mv/ms	47.3 ± 24.2 (39)	16.3 to 118
Fast afterhyperpolarization		
Amplitude, mV	15.1 ± 3.7 (26)	6.7 to 21.1
Half-decay, ms	80.8 ± 34.9 (26)	28.6 to 152
Duration, ms	230 ± 71 (26)	109 to 363
Slow afterhyperpolarization		
Amplitude, mV	8.3 ± 4.5 (30)	2.8 to 18.4
Half-decay, ms	358 ± 223 (30)	101 to 1097
f-I slope		
Maximal, Hz/pA	0.126 ± 0.033 (39)	0.06 to 0.20
Sustained, Hz/pA	0.075 ± 0.025 (39)	0.03 to 0.13

		r	R^2	n	p
Membrane properties					
R_{in}	τ_m	0.82	0.68	38	$2.5 \cdot 10^{-10}$•
"	C_m	−0.09	0.01	"	0.58
τ_m	C_m	0.44	0.19	"	0.0057
Rheobase					
I_{rheo}	V_{hold}	−0.20	0.04	39	0.23
"	g_{in} (R_{in}^{-1})	0.60	0.36	38	$6.8 \cdot 10^{-5}$•
"	τ_m^{-1}	0.48	0.23	"	0.0024
"	C_m	0.04	0.00	"	0.79
$I_{rheo} \cdot R_{in}$	V_{th}	0.64	0.41	"	$1.5 \cdot 10^{-5}$•
Firing frequency					
f_{max} @ 100pA	R_{in}	0.51	0.26	30	0.0036
f_{sus} @ 100pA	R_{in}	0.43	0.19	"	0.016
f_{max}-I slope	R_{in}	0.49	0.24	38	0.0018
"	I_{rheo}	−0.49	0.24	39	0.0017*
"	τ_m	0.21	0.04	38	0.21
"	C_m	−0.31	0.10	"	0.058
f_{sus}-I slope	R_{in}	0.44	0.19	"	0.0059
"	I_{rheo}	−0.52	0.27	39	$7.5 \cdot 10^{-4}$•
"	τ_m	0.24	0.06	38	0.15
"	C_m	−0.27	0.07	"	0.11
Afterhyperpolarization					
fAHP half-decay	fAHP duration	0.86	0.73	26	$2.5 \cdot 10^{-8}$•
"	R_{in}	0.31	0.10	"	0.12
"	C_m	0.25	0.06	"	0.22
"	τ_m	0.46	0.21	"	0.019
"	I_{rheo}	−0.52	0.27	"	0.0064
"	f_{max} @ $2 \cdot I_{rheo}$	−0.77	0.59	"	$8.6 \cdot 10^{-5}$•
"	f_{sus} @ $2 \cdot I_{rheo}$	−0.65	0.43	25	$3.9 \cdot 10^{-4}$•
"	f_{max}-I slope	−0.01	0.00	26	0.95
"	f_{sus}-I slope	0.46	0.21	"	0.019
"	sAHP half-decay	−0.38	0.14	19	0.11
sAHP half-decay	SRA ratio	0.52	0.27	28	0.0045

	Type 1	Type 2	Type 3	
Membrane properties				
RMP, mV	-58.7 ± 7.8 (22)	-57.5 ± 6.2 (13)	-63.0 ± 6.8 (4)	$F_{(2,36)}$=.87 p=0.43
R_{in}, MΩ	1070 ± 603 (22)	1006 ± 525 (12)	1285 ± 381 (4)	$F_{(2,35)}$=0.37 p=0.69
τ_m, ms	100.0 ± 59.7 (22)	85.0 ± 55.3 (12)	90.8 ± 16.5 (4)	$F_{(2,35)}$=0.29 p=0.75
C_m, pF	95.1 ± 28.9 (22)	83.7 ± 23.7 (12)	73.0 ± 15.4 (4)	$F_{(2,35)}$=1.6 p=0.23
Threshold				
Absolute, mV	-42.2 ± 7.1 (22)	-38.9 ± 7.7 (13)	-43.2 ± 4.2 (4)	$F_{(2,36)}$=1.0 p=0.36
Relative, mV	26.7 ± 8.0 (22)	25.5 ± 7.1 (13)	23.6 ± 9.1 (4)	$F_{(2,36)}$=0.31 p=0.74
Rheobase, pA	30.1 ± 17.3 (22)	26.2 ± 13.3 (13)	17.5 ± 15.5 (4)	$F_{(2,36)}$=1.1 p=0.33
Action potential				
Amplitude, mV	48.1 ± 14.8^{a} (22)	67.3 ± 11.6^{b} (13)	52.6 ± 6.6 (4)	$F_{(2,36)}$=8.5 p=0.00092
Peak, mV	6.0 ± 18.0^{a} (22)	28.3 ± 10.4^{b} (13)	9.4 ± 9.3 (4)	$F_{(2,36)}$=9.0 p=0.00069
Half-width, ms	5.1 ± 1.1^{a} (22)	3.8 ± 0.7^{b} (13)	4.4 ± 0.5 (4)	$F_{(2,36)}$=8.5 p=0.00092
Rise slope, mV/ms	35.9 ± 18.2^{a} (22)	68.7 ± 22.8^{b} (13)	41.0 ± 6.8^{a} (4)	$F_{(2,36)}$=12.1 p=$9.6 \cdot 10^{-5}$
fAHP				
Amplitude, mV	-14.3 ± 3.1 (15)	-16.8 ± 4.5 (9)	-13.3 ± 3.2 (2)	$F_{(2,33)}$=1.5 p=0.24
Half-decay, ms	89.1 ± 28.3 (15)	65.9 ± 38.3 (9)	85.8 ± 66.3 (2)	$F_{(2,23)}$=1.3 p=0.29
Duration, ms	252 ± 61 (15)	205 ± 76 (9)	181 ± 101 (2)	$F_{(2,33)}$=1.9 p=0.18

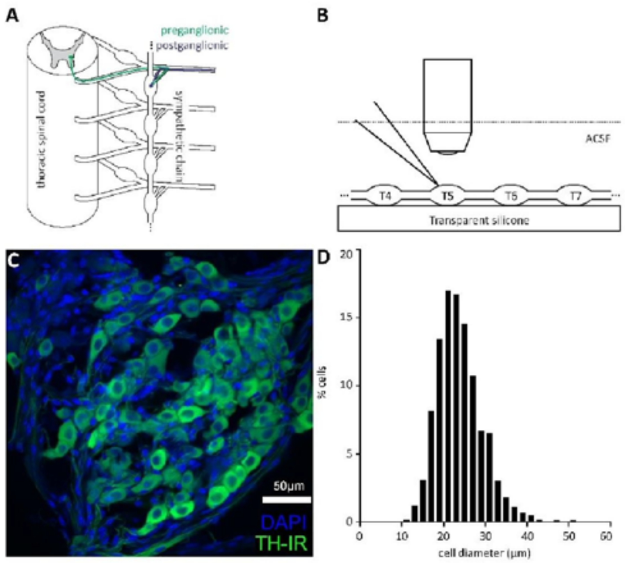
A
preganglionic
postganglionic
thoracic spinal cord
sympathetic chain
B
ACSF
T4
T5
T6
T7
Transparent silicone
C
50µm
DAPI
TH-IR
D
% cells
cell diameter (µm)

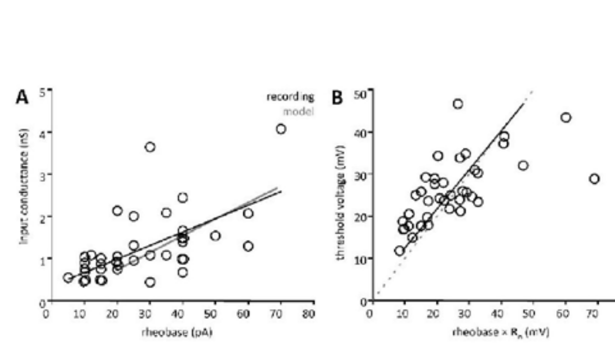
A
recording
model
input conductance (nS)
rheobase (pA)
B
threshold voltage (mV)
rheobase × R_N (mV)

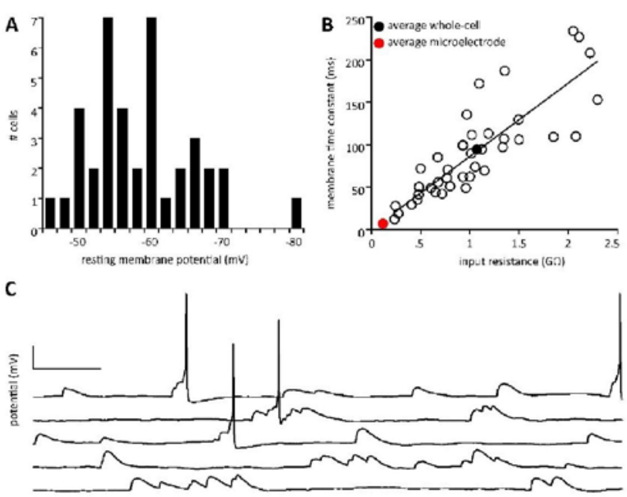
A
cells
resting membrane potential (mV)
B
average whole-cell
average microelectrode
membrane time constant (ms)
input resistance (GΩ)
C
potential (mV)

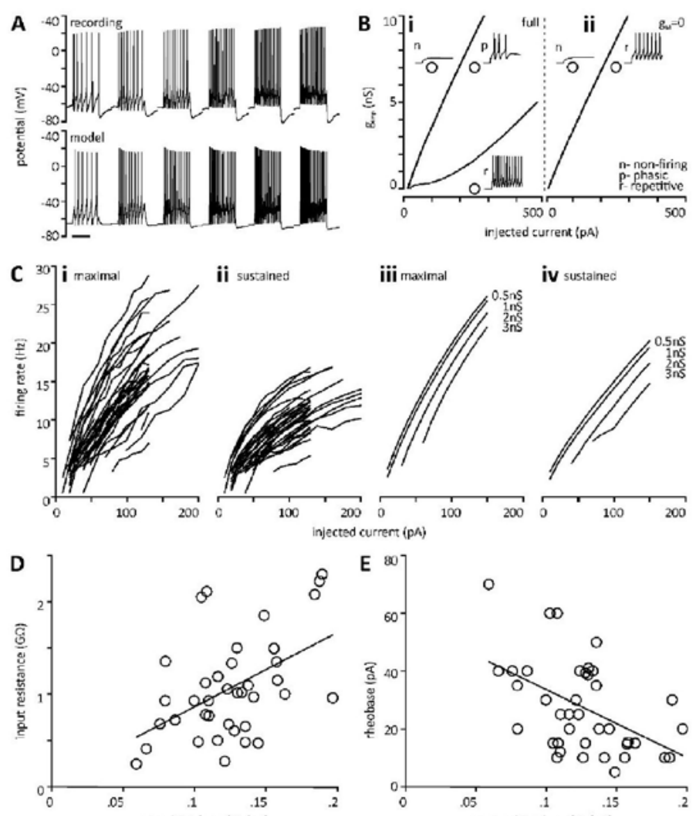
A
recording
model
potential (mV)
B
i
full
ii
n
p
r
n- non-firing
p- phasic
r- repetitive
injected current (pA)
C
i maximal
ii sustained
iii maximal
iv sustained
0.5nS
1nS
2nS
3nS
firing rate (Hz)
injected current (pA)
D
input resistance (GΩ)
maximal F-I slope (Hz/pA)
E
rheobase (pA)
maximal F-I slope (Hz/pA)

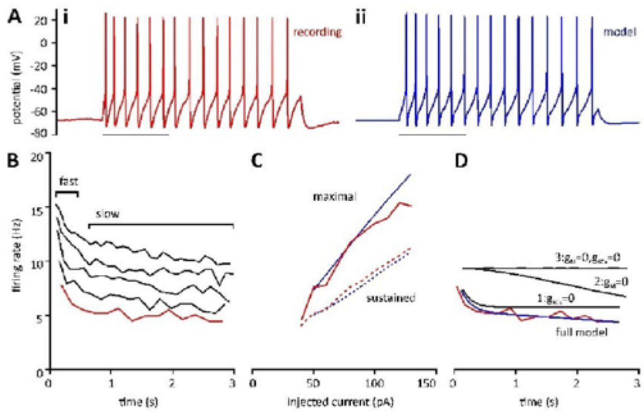
A
i
ii
recording
model
potential (mV)
B
C
D
fast
slow
firing rate (Hz)
time (s)
maximal
sustained
injected current (pA)
full model
time (s)

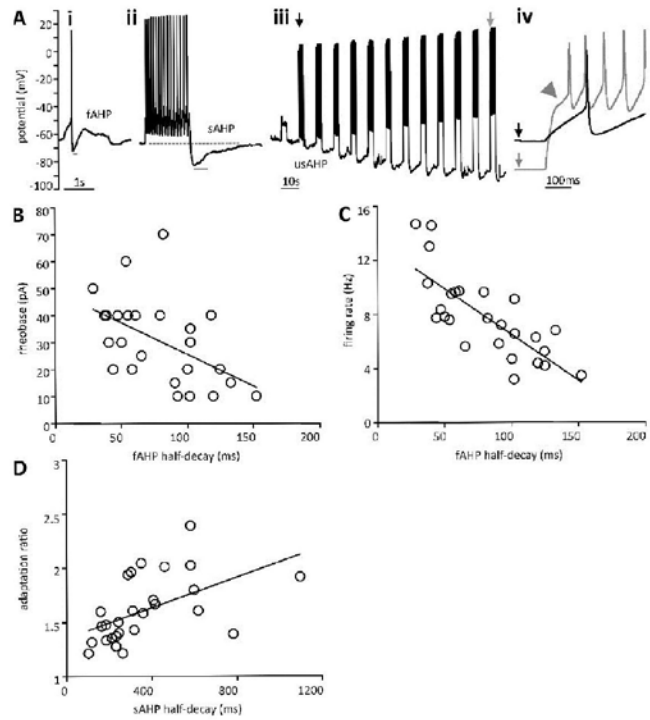
A
i
ii
iii
iv
potential (mV)
fAHP
sAHP
usAHP
1s
10s
100ms
B
C
D
rheobase (pA)
fAHP half-decay (ms)
firing rate (Hz)
fAHP half-decay (ms)
adaptation ratio
sAHP half-decay (ms)

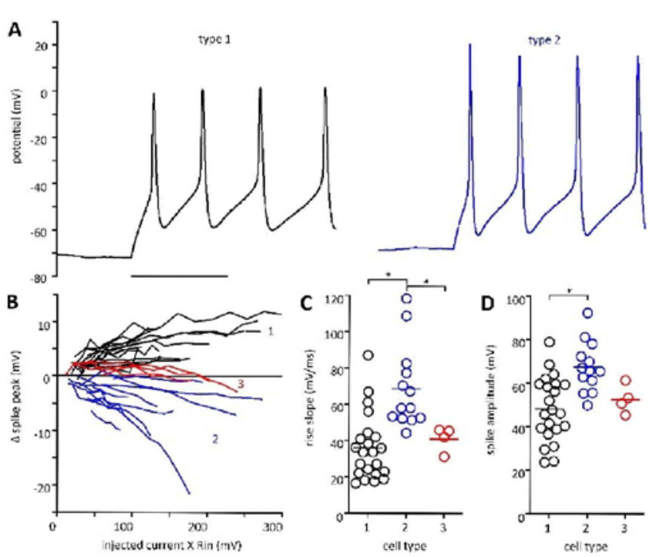
A
type 1
type 2
potential (mV)
B
Δ spike peak (mV)
injected current X Rin (mV)
C
rise slope (mV/ms)
cell type
D
spike amplitude (mV)
cell type

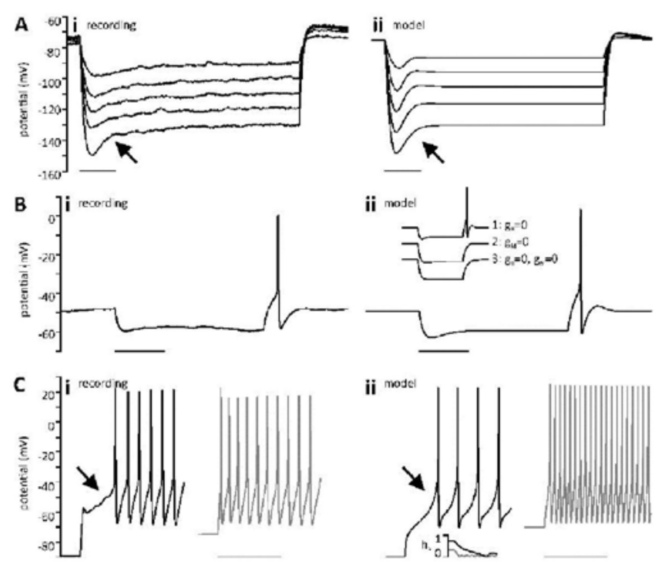
A
i
recording
ii
model
potential (mV)
B
i
recording
ii
model
potential (mV)
C
i
recording
ii
model
potential (mV)

h. posters

Experimental Biology Annual Meeting 2018

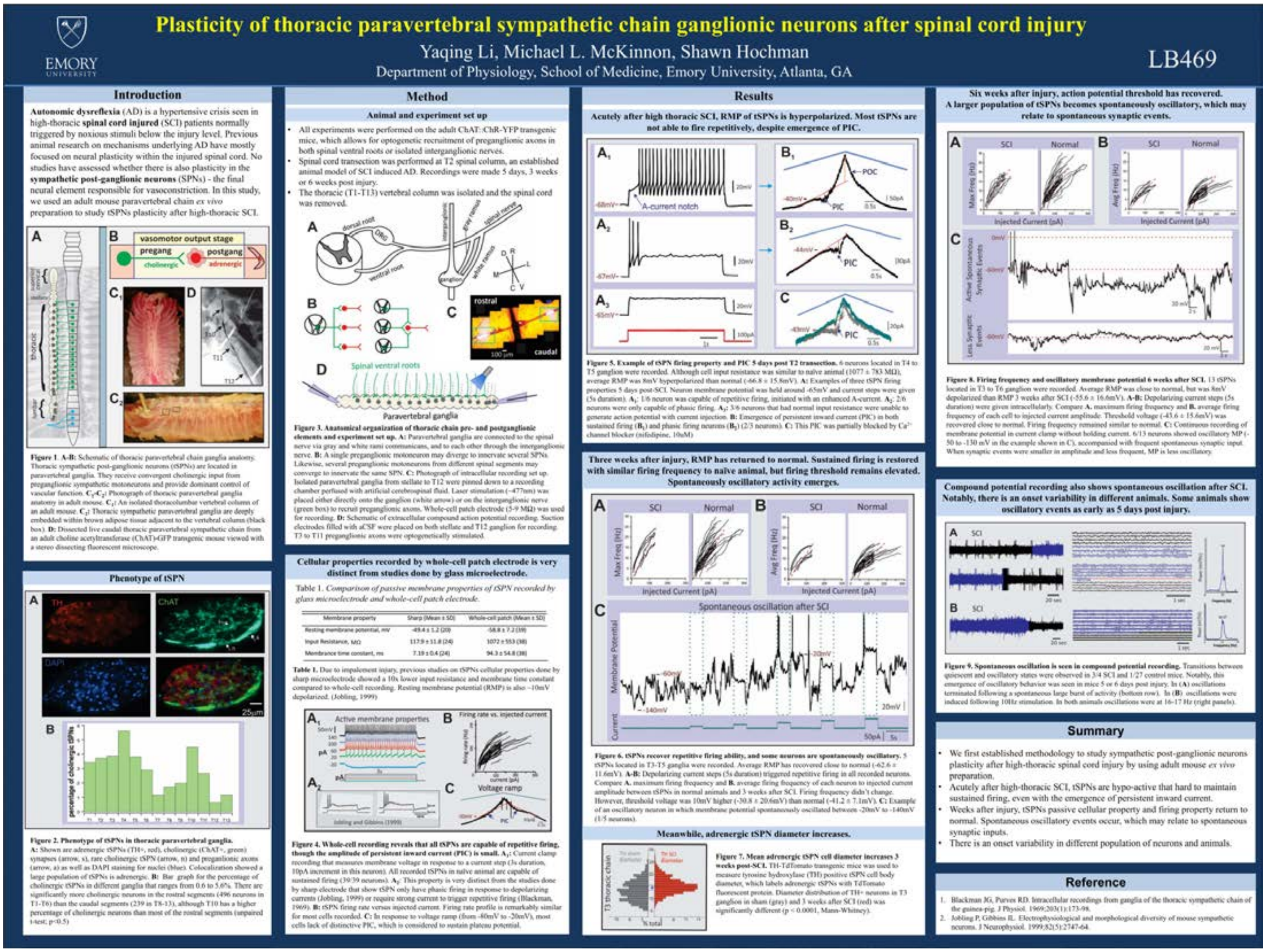

Society for Neuroscience Annual meeting 2018

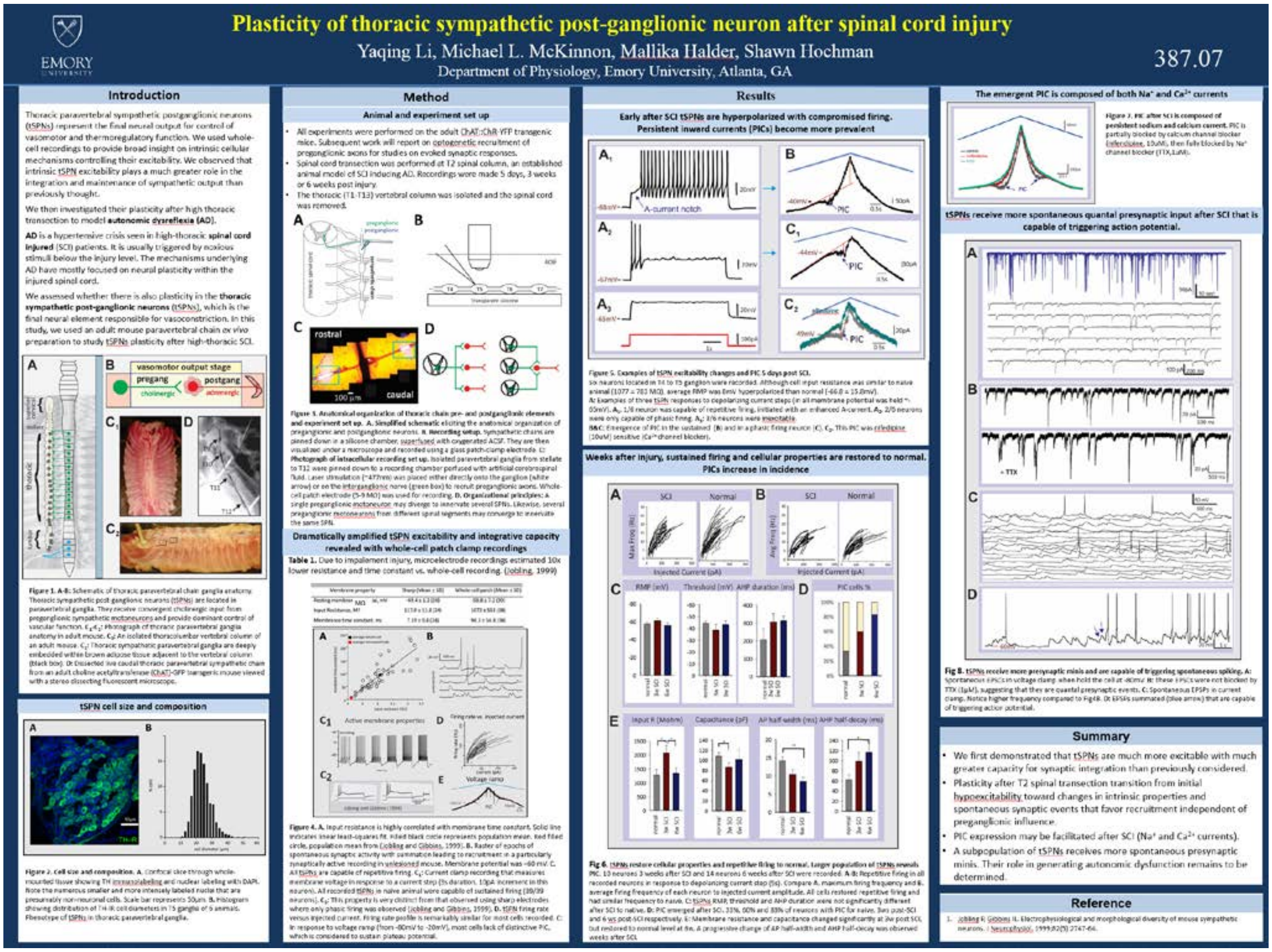
Plasticity of thoracic sympathetic post-ganglionic neuron after spinal cord injury
Yaqing Li, Michael L. McKinnon, Mallika Halder, Shawn Hochman
Department of Physiology, Emory University, Atlanta, GA
387.07
EMORY UNIVERSITY
Introduction
Method
Animal and experiment set up
Results
Early after SCI tSPNs are hyperpolarized with compromised firing. Persistent inward currents (PICs) become more prevalent
Weeks after injury, sustained firing and cellular properties are restored to normal. PICs increase in incidence
The emergent PIC is composed of both Na+ and Ca2+ currents
tSPN cell size and composition
Dramatically amplified tSPN excitability and integrative capacity revealed with whole-cell patch clamp recordings
tSPNs receive more spontaneous quantal presynaptic input after SCI that is capable of triggering action potential.
Summary
We first demonstrated that tSPNs are much more excitable with much greater capacity for synaptic integration than previously considered.
Plasticity after T2 spinal transection transition from initial hypoexcitability toward changes in intrinsic properties and spontaneous synaptic events that favor recruitment independent of preganglionic influence.
PIC expression may be facilitated after SCI (Na+ and Ca2+ currents).
A subpopulation of tSPNs receives more spontaneous presynaptic minis. Their role in generating autonomic dysfunction remains to be determined.
Reference

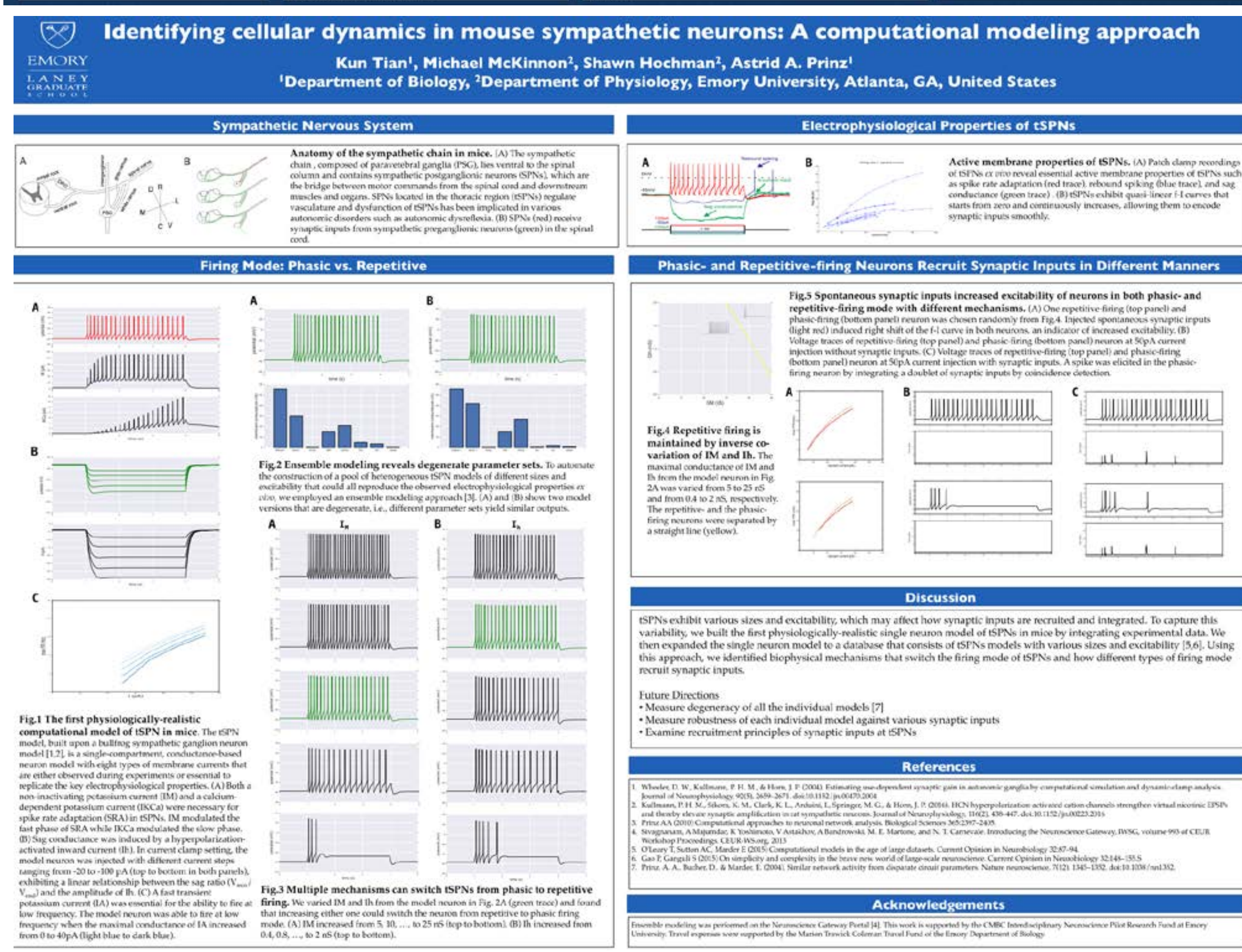
Identifying cellular dynamics in mouse sympathetic neurons: A computational modeling approach
Kun Tian1, Michael McKinnon2, Shawn Hochman2, Astrid A. Prinz1
1Department of Biology, 2Department of Physiology, Emory University, Atlanta, GA, United States
EMORY LANEY GRADUATE SCHOOL
Sympathetic Nervous System
Electrophysiological Properties of tSPNs
Firing Mode: Phasic vs. Repetitive
Phasic- and Repetitive-firing Neurons Recruit Synaptic Inputs in Different Manners
Discussion
tSPNs exhibit various sizes and excitability, which may affect how synaptic inputs are recruited and integrated. To capture this variability, we built the first physiologically-realistic single neuron model of tSPNs in mice by integrating experimental data. We then expanded the single neuron model to a database that consists of tSPNs models with various sizes and excitability [5,6]. Using this approach, we identified biophysical mechanisms that switch the firing mode of tSPNs and how different types of firing mode recruit synaptic inputs.
Future Directions
• Measure degeneracy of all the individual models [7]
• Measure robustness of each individual model against various synaptic inputs
• Examine recruitment principles of synaptic inputs at tSPNs
References
Acknowledgements